Gondwana Research 70 (2019) 151–170

Contents lists available at ScienceDirect

Gondwana Research

journal homepage: www.elsevier.com/locate/gr

Cambrian intra–oceanic arc trondhjemite and tonalite in the Tam Ky–Phuoc Son Suture Zone, central Vietnam: Implications for the early Paleozoic assembly of the Indochina Block

Quyen Minh Nguyen [a,b,c], Qinglai Feng [a,b,*], Jian-Wei Zi [a,d], Tianyu Zhao [a,b], Hai Thanh Tran [c], Thanh Xuan Ngo [c], Dung My Tran [e], Hung Quoc Nguyen [c]

[a] State Key Laboratory of Geological Processes and Mineral Resources, China University of Geosciences, Wuhan 430074, China
[b] School of Earth Sciences, China University of Geosciences, Wuhan 430074, China
[c] Department of Geology, Hanoi University of Mining and Geology, Hanoi, Viet Nam
[d] John de Laeter Centre, Curtin University, Perth, WA 6102, Australia
[e] General Department of Geology and Minerals of Viet Nam, Hanoi, Viet Nam

ARTICLE INFO

Article history:
Received 7 July 2018
Received in revised form 11 January 2019
Accepted 12 January 2019
Available online 30 January 2019

Handling Editor: S. Kwon

Keywords:
Gondwana
Tectonic evolution
Zircon U–Pb dating
Zircon Hf isotope
Geochemistry

ABSTRACT

The Truong Son and Kon Tum terranes in northeastern Indochina are thought to, respectively, form part of the Indian and Australian margins of Gondwana and separated one another by the Tam Ky–Phuoc Son Ocean during the early Paleozoic. In this paper, we present results of a comprehensive geochronological and geochemical study on a trondhjemite–tonalite suite identified in the Tam Ky–Phuoc Son Suture Zone. LA–ICP–MS zircon U–Pb dating yielded weighted mean $^{206}Pb/^{238}U$ ages of 518.5 ± 7.1 Ma and 502.1 ± 6.0 Ma for the trondhjemite and tonalite, respectively. These are the oldest magmatic zircons recorded in this area so far. Both rocks consist primarily of plagioclase (oligoclase), quartz, with minor, variable amounts of hornblende and biotite. They have high SiO_2, Na_2O and Y, but low Al_2O_3, K_2O, Sr and Rb contents, and are characterized by depletion in LREEs with flat HREE patterns. These features are similar to those of typical oceanic plagiogranites. Our new evidences from field geology, geochemistry, and zircon Hf isotopic data, along with previously published data from the Tam Ky–Phuoc Son Suture Zone, suggest that the plagiogranites were originated from extensive fractionation of hydrous basaltic magmas. Furthermore, they were generated in an intra-oceanic arc system above a northward subduction zone within the Tam Ky–Phuoc Son Ocean. The final closure of this ocean took place before the late Silurian, marked by collision of the Truong Son Terrane with the Kon Tum Terrane along the Tam Ky–Phuoc Son Suture Zone to form the Indochina Block. After elimination of the southeastward offset along the Red River shear zone and the clockwise rotation of Indochina relative to South China since the Tertiary, the eastern part of the Tam Ky–Phuoc Son Suture aligns well with the Kuungan Suture on Hainan Island, together they have likely recorded the final assembly of Gondwana in this region.

© 2019 International Association for Gondwana Research. Published by Elsevier B.V. All rights reserved.

1. Introduction

The Indochina, South China, South Qiangtang, North China, Tarim, Lhasa, and Sibumasu blocks have been considered as continental fragments that were distributed around the northern margin of Gondwana during the early Paleozoic (e.g., Cocks and Torsvik, 2013; Metcalfe, 2013; Cawood et al., 2017; Zhao et al., 2017). However, the precise paleo–position of the Indochina Block during the early Paleozoic is a highly controversial issue, perhaps one of the biggest unsolved problems of eastern Asian paleogeography (Cocks and Torsvik, 2013). Metcalfe (2011, 2013) placed the Indochina Block adjacent to the Australian margin of Gondwana mainly based on the presence of granulites in the Kon Tum Terrane (KT), central Vietnam (Fig. 1), which has been suggested to form part of the Gondwana granulite belt (Katz, 1993). By contrast, some other workers have used detrital zircon data from the Truong Son Terrane (TST) to deduce that the Indochina Block was near the Indian margin of Gondwana (e.g., Usuki et al., 2013; Burrett et al., 2014; C. Wang et al., 2016). Such interpretive discrepancy is likely related to the fact that the TST was separated from Kon Tum by an ocean represented by the Tam Ky–Phuoc Son Suture Zone (TPSZ) during the early Paleozoic (e.g., Tran et al., 2014; Shi et al., 2015; Gardner et al., 2017) (Fig. 1).

The E–W trending TPSZ is located in the northeastern part of the Indochina Block, extending >100 km from Tamky to Phuocson in central

* Corresponding author at: State Key Laboratory of Geological Processes and Mineral Resources, China University of Geosciences, Wuhan 430074, China.
E-mail address: qinglaifeng@cug.edu.cn (Q. Feng).

https://doi.org/10.1016/j.gr.2019.01.002
1342-937X/© 2019 International Association for Gondwana Research. Published by Elsevier B.V. All rights reserved.

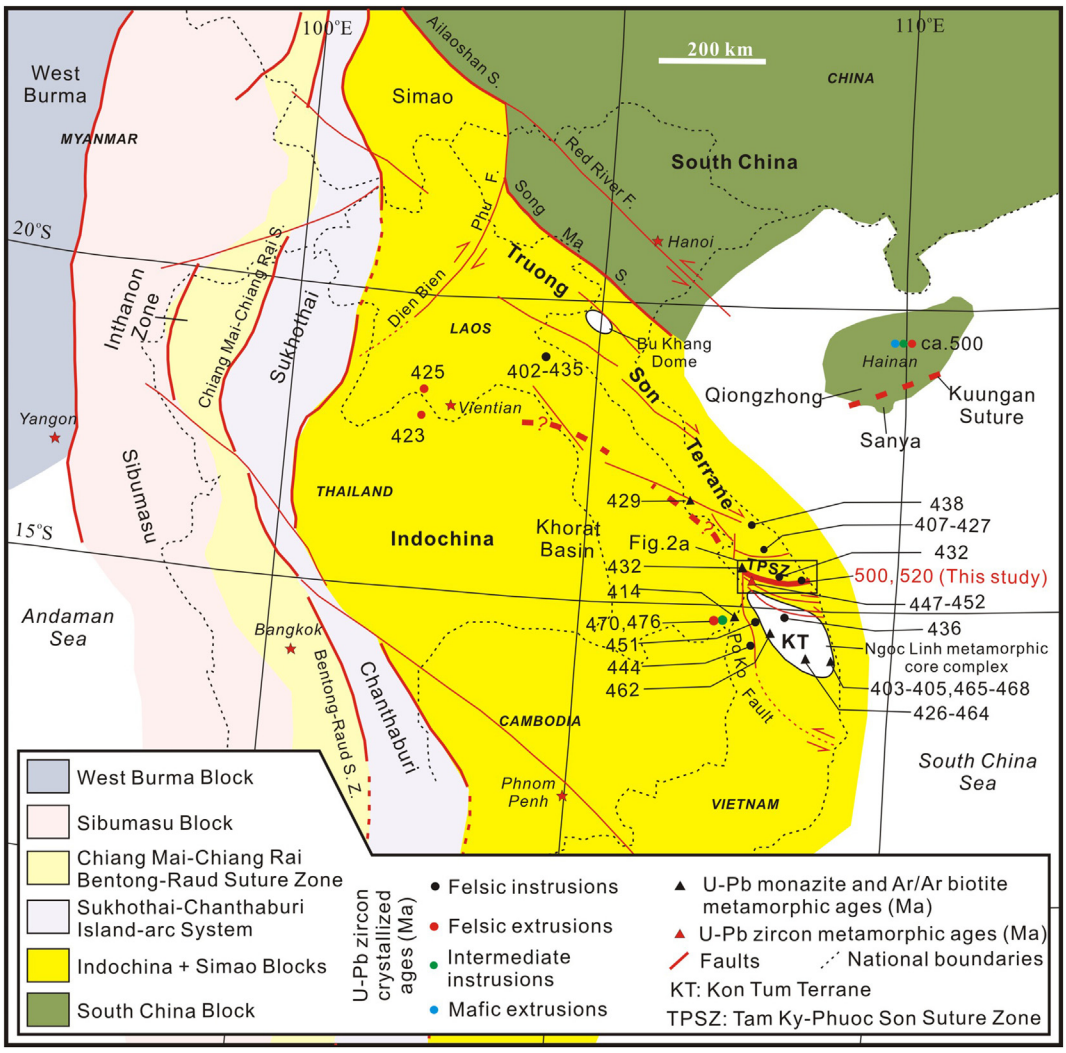

Fig. 1. Simplified tectonic map of Southeast Asia (after Jolivet et al., 2001; Lepvrier et al., 2004; Xu et al., 2014; Cawood et al., 2017; Metcalfe et al., 2017; Faure et al., 2018). The ages of magmatic and metamorphic rocks are from: Carter et al., 2001; Nagy et al., 2001; Ding et al., 2002; Maluski et al., 2005; Roger et al., 2007; Xu et al., 2007; Usuki et al., 2009; Nakano et al., 2013; Tran et al., 2014; Shi et al., 2015; Hieu et al., 2016; S.F. Wang et al., 2016; Zhao et al., 2016; Gardner et al., 2017.

Vietnam (e.g., Tran et al., 2014) (Figs. 1, 2a). Within this zone, there occur numerous lenticular–shaped, a few meters to several kilometers long, metamorphosed peridotites (dunite and harzburgite), cumulate gabbros–pyroxenites, gabbros, and plagiogranites. It is observed that the peridotites and gabbros are locally cross–cut by doleritic dykes. All these rocks are sandwiched between, or tectonically juxtaposed by, foliated meta–extrusive (mafic to felsic) rocks that are intercalated with marbles, meta–siliceous shales, metapelites and metagreywackes (e.g., Nguyen, 1986; Nguyen, 2001; Huynh et al., 2009; Tri and Khuc, 2011). Dung et al. (2006) and Izokh et al. (2006) suggested that some of these rocks bear characteristics of ophiolites. Recent structural studies (Tran et al., 2014, 2016) have also presented persuasive evidence for terrane assembly along the TPSZ. However, the igneous rocks in this suture are still poorly understood with regard to their petrogenesis and formation ages. Tri and Khuc (2011) tentatively assigned an early Paleozoic age to the metamorphosed mafic–ultramafic suite based on an Early Ordovician age (whole–rock Rb–Sr isochron method) obtained for the meta–basalts and the cross–cutting relationship with the surrounding rocks. Similarly, some intermediate to felsic intrusive complexes scattered along the TPSZ are also believed to have emplaced in the early Paleozoic or late Ordovician–early Silurian (Nguyen, 1986; Tri and Khuc, 2011), although direct age constraints are lacking. The only temporally well–constrained magmatic rocks are the ca. 430–400 Ma granites that cross–cut the TPSZ (e.g., Tran et al., 2014; Nguyen and Tran, 2016).

In the present paper, we review previously published data from the TPSZ area, and present new results of a comprehensive study involving whole–rock geochemistry, zircon U–Pb geochronology and Hf isotopes, zircon and plagioclase geochemistry for oceanic plagiogranites in the TPSZ with aims to better constrain the origin, tectonic setting, and emplacement ages of these rocks. The new data provide invaluable insights into the configuration and formation history of the TPSZ and Indochina Block in the context of Gondwana evolution.

2. Geological setting

The Indochina Block is separated from the South China, Simao and Sibumasu blocks by the Song Ma Suture, Dien Bien Phu Fault, and Chiang Mai–Chiang Rai–Bentong–Raub Suture in the northeast, northwest and west–southwest, respectively. However, the eastern boundary of this block is poorly defined but has been suggested to be immersed in the South China Sea (Fig. 1) (e.g., Metcalfe, 2013, Metcalfe et al., 2017; Bui et al., 2017). The TST and KT are located in the northeastern part of the Indochina Block, and are separated by the TPSZ (Fig. 1).

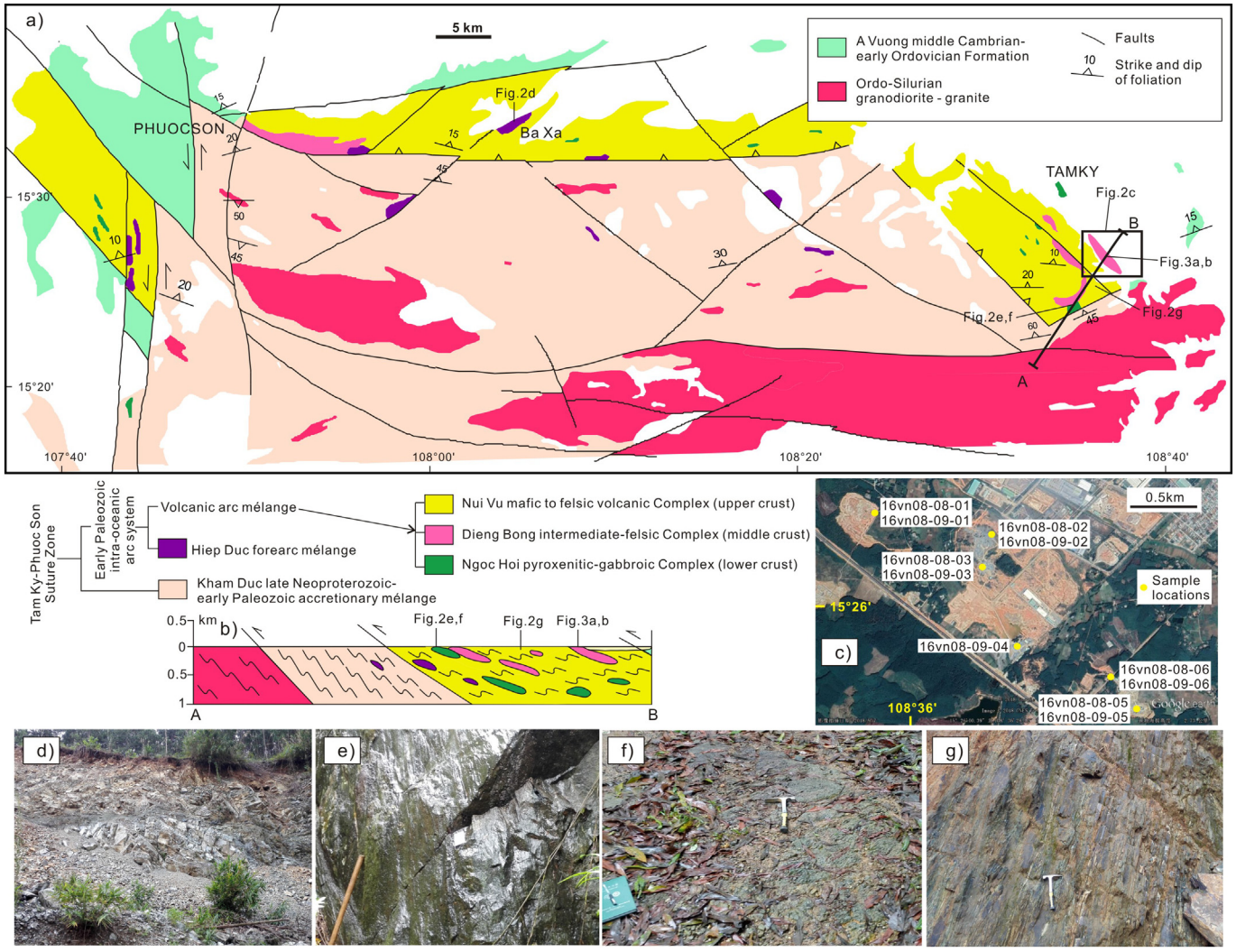

Fig. 2. (a) Simplified geological map of the study area in central Vietnam showing distribution of the Tam Ky–Phuoc Son Suture Zone, and (b) a cross–section showing elements of this suture based on a compilation of (Nguyen, 1986; Nguyen, 2001); (c) the inset map displays all sample locations; field photographs of (d) the Hiep Duc highly serpentinized meta–peridotite, (e) Ngoc Hoi cumulate pyroxenite, (f) Ngoc Hoi cumulate gabbro, and (g) Nui Vu meta–siliceous shale and volcanogenic metapelite.

2.1. The Truong Son Terrane

The Precambrian lower continental crust of the TST is represented by the over 4500 m thick biotite–sillimanite–disthene–garnet schists and amphibolites of the Bu Khang Dome in northern central Vietnam (Fig. 1), which was exhumed during the Oligocene–Miocene by northeast–southwest extension associated with the opening of the South China Sea (e.g., Jolivet et al., 1999, 2001). This crystalline basement is mainly covered by Paleozoic to Mesozoic volcano–sedimentary rocks that were intruded by plutonic rocks of different ages (e.g., Tri and Khuc, 2011).

2.2. The Kon Tum Terrane

The granulites within the Ngoc Linh metamorphic core complex of the KT in central Vietnam have been regarded as an exposed Archean core complex of the Indochina Block (e.g., DGMVN, 1989; Hutchison, 1989; Metcalfe et al., 2017) (Fig. 1). However, the only late Archean age that has been recorded is a Nd model age of 2.7 Ga for a pelitic granulite, which has trace element signatures similar to that of the lower continental crust (Lan et al., 2003). Instead, it has been suggested that the KT basement was principally formed during the Proterozoic (e.g., Lan et al., 2003; Owada et al., 2007, 2016), and has been reworked by at least two high–grade metamorphic events during the Ordo–Silurian (e.g., Nakano et al., 2013; Tran et al., 2014) and Permo–Triassic (e.g., Nakano et al., 2007; Sanematsu et al., 2011; Faure et al., 2018). The basement is partly covered by Mesozoic volcano–sedimentary formations, Neogene–Quaternary basaltic extrusive rocks, and is intruded by Paleo–Mesozoic igneous bodies (e.g., Hoang and Flower, 1998; Tri and Khuc, 2011). Because of the dense covering of younger rocks, the western and southwestern parts of the KT are not well defined. However, the migmatite widely occurs west of the Po Ko Neogene sinistral strike–slip fault in the Laos territory (e.g., Faure et al., 2018), indicating that the KT likely be northwestward extended under the Mesozoic (e.g., Carter and Bristow, 2003) Khorat Basin (Fig. 1).

2.3. The Tam Ky–Phuoc Son Suture Zone

There are five rock associations within the TPSZ, namely: the Kham Duc volcano–sedimentary Complex, the Hiep Duc ultramafic–mafic Complex, the Ngoc Hoi pyroxenitic–gabbroic Complex, the Dieng Bong intermediate–felsic Complex and the Nui Vu mafic to felsic volcanic Complex (e.g., Nguyen, 1986; Nguyen, 2001; Huynh et al., 2009) (Fig. 2). All rocks have undergone multiple episodes of ductile to brittle deformation, and have been metamorphosed to greenschist to granulite

facies (e.g., Lepvrier et al., 1997; Lepvrier et al., 2004; Tran et al., 2014, 2016; Faure et al., 2018).

Rocks of the late Neoproterozoic–early Paleozoic (e.g., Usuki et al., 2009; Tri and Khuc, 2011, p. 53) Kham Duc Complex are largely distributed in the center and southern part of the study area (Fig. 2a, b). They are characterized by meta–volcanic rocks in the lower part, marble and metapelite intercalated with meta–volcanic rocks in the middle part, and dominated by metapelite, metagreywacke in the upper part. Repeated deformation (Tran et al., 2014, 2016) had led to overthickening of the formation to 5000–5800 m (Nguyen, 1986). The Kham Duc rocks have experienced amphibolite– to granulite–facies metamorphism under moderate–pressure conditions (Nakano et al., 2009, 2013; Usuki et al., 2009). The meta–volcanic rocks show subduction–related geochemical features (e.g., Nguyen, 2001). Collectively, all these evidences are in favor of an accretionary mélange, which belongs to the TPSZ, for the Kham Duc rocks (e.g., Faure et al., 2018).

The Hiep Duc Complex is best exposed in the Ba Xa area (Fig. 2a, d). It consists of numerous lenticular–shaped, strongly serpentinized, upper mantle meta–peridotites (dunite and harzburgite), which locally include the disseminated chromites. Meta–gabbros, meta–basalts, meta–andesites, quartzitized cherts, and thin–bedded marbles also occur in this complex. In places, isolated meta–diabases are seen to crosscut the meta–peridotites and meta–gabbros (e.g., Izokh et al., 2006; Dung et al., 2006). The Hiep Duc Complex locally exhibits the pseudostratigraphy of a complete Penrose–type oceanic crust, and is interpreted herein as representing an intra–oceanic forearc remnant [i.e., forearc ophiolite (e.g., Dilek and Furnes, 2011, 2014)] (see more details in Section 6. Discussion).

The 1200–1600 m thick Nui Vu volcanic Complex is striking northwest–southeast to nearly east–west, and can be subdivided into lower and upper parts. The lower part is composed mainly of meta–extrusive (mafic to felsic, mostly intermediate) rocks intercalated with minor meta–siliceous shale and volcanogenic metapelite, whereas the upper part consists predominantly of volcanogenic metapelite with less meta–extrusive intercalations (Fig. 2a, g). The Ngoc Hoi Complex is characterized by metamorphosed cumulate pyroxenite–gabbro, pyroxentite and gabbro (Fig. 2e, f), whereas the Dieng Bong Complex is constituted by meta–trondjemite–tonalite–diorite (Fig. 3a, b). The intrusions of these two complexes usually form small to moderate (from <1 to over 20 km^2) stratiform– or lenticular–shaped bodies that display oriented structures, and are conformably distributed within surrounding foliated metamorphic rocks of the Nui Vu volcanic Complex (e.g., Tri and Khuc, 2011, p. 51). Previous geochemical studies (e.g., Nguyen, 1986; Nguyen, 2001) have indicated that all the volcanic and intrusive rocks show calc–alkaline affinity with depletion in HFSEs and enrichment in LILEs, and were most likely formed in a subduction–related setting. In summary, all the three rock associations have structural, compositional and sedimentological (i.e., mainly

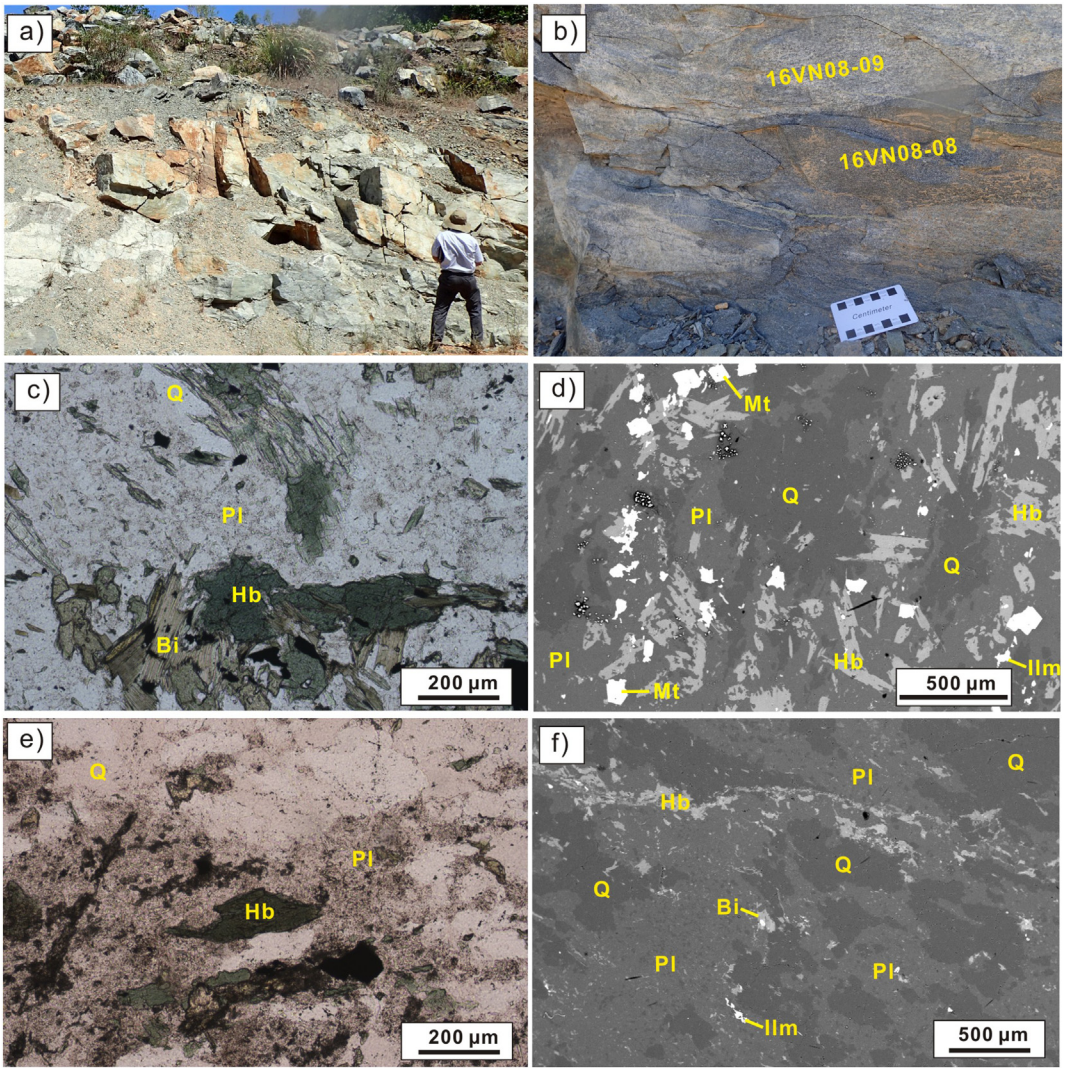

Fig. 3. (a) Outcrop photograph of Dieng Bong Complex; (b) close–up photograph of the 16VN08–08 and 16VN08–09 samples, note their sharp contact; (c) optical and (d) SEM photographs of 16VN08–08 samples; (e) optical and (f) SEM photographs of 16VN08–09 samples; Q–quartz, Pl–plagioclase, Hb–hornblende, Bi–biotite, Mt–magnetite, Ilm–ilmenite.

deep–water and arc–derived sediments in volcanic complex) features similar to the typical modern intra–oceanic volcanic arc crust (Stern, 2010), with the Ngoc Hoi pyroxenitic–gabbroic Complex, Dieng Bong intermediate–felsic Complex, and Nui Vu mafic to felsic volcanic Complex corresponding to the lower, middle and upper arc crusts, respectively.

In summary, the TPSZ consists of three distinct mélange units, including, from south to north, an accretionary mélange (i.e., the Kham Duc Complex), an intra–oceanic forearc mélange (i.e., the Hiep Duc Complex) and an intra–oceanic volcanic arc mélange (i.e., the Ngoc Hoi, Dieng Bong, Nui Vu Complexes) (Fig. 2a).

2.4. The surrounding areas of the TPSZ

The middle Cambrian–early Ordovician (Tri and Khuc, 2011, p. 59; C. Wang et al., 2016) A Vuong Formation crops out mostly at northern part of the study area, and has tectonic contact with rocks of the TPSZ (Fig. 2a, b). It is 1800–2900 m thick, composed largely of terrigenous, terrigeno–carbonate, rich in carbonaceous schist with minor altered mafic to felsic volcanics, located next to the TPSZ, and all rocks have been metamorphosed to the greenschist facies. The mafic to felsic volcanic rocks is likely related to the TPSZ. However, the thick, shallow–water sediments were deposited over a long period, indicating that the A Vuong Formation might have formed in a passive continental margin setting (Nguyen, 2001).

Ordo–Silurian granodioritic intrusions (e.g., Faure et al., 2018; authors' unpublished data) are widely distributed in the southern part, and are parallel to the predominant regional structural orientation (Fig. 2a). Generally, these rocks belong to peraluminous, calc–alkaline series with enrichment in LILEs and depletion in HFSEs (e.g., Tri and Khuc, 2011, p. 240–244). They have been interpreted to have formed either in extensive (e.g., Carter et al., 2001; Lan et al., 2003) or in compressive (e.g., Usuki et al., 2009; Tran et al., 2014) settings.

3. Sample locations and petrography

A number of pyroxenitic, gabbroic and intermediate–felsic intrusions of the Ngoc Hoi and Dieng Bong complexes are exposed in the study area and are tectonically incorporated within the Nui Vu volcanic Complex (Fig. 2a). Five trondhjemite–tonalite–diorite bodies of the Dieng Bong Complex with areal extent of 0.5 to 20 km^2 have been mapped (e.g., Nguyen, 1986; Nguyen, 2001) (Fig. 2a). Five gray–colored (16VN08–08–01, –02, –03, –05, –06) and six grayish white–colored samples (16VN08–09–01, –02, –03, –04, –05, –06) were collected from the best exposed intrusive body (ca. 5 km^2) near Tam Ky Town (Fig. 2a, c) for whole–rock geochemical studies. Among them two samples (16VN08–08–06, 16VN08–09–06) (15°25′38.46″N, 108°36′50.03″E) were selected for zircon U–Pb dating, Lu–Hf isotopic composition and mineral geochemistry.

The gray– and grayish white–colored rocks (16VN08–08 and 16VN08–09 samples, respectively) appear to be closely associated with each other, but are separated by a clear boundary between them (Fig. 3b). Petrographic observations under optical and scanning electron microscopes indicate that both rocks are characterized by strongly deformed plagioclase, quartz and amphibole (Fig. 3). The 16VN08–08 samples display gneissic texture. They are mainly composed of plagioclase (50–60%), quartz (15–25%), hornblende (10–20%) and biotite (0–2%). Plagioclase is mostly oligoclase in composition, and locally altered to sericite. Hornblende is subhedral and altered to chlorite and epidote. Accessory minerals include magnetite, pyrite, ilmenite, apatite, sphene and zircon (Fig. 3c, d). The 16VN08–09 samples also have gneissic texture. They consist mainly of plagioclase (50–60%), quartz (25–35%), hornblende (1–10%) and biotite (0–1%). Plagioclase is mainly oligoclase in composition, and locally altered to sericite. Hornblende is subhedral, and is partially altered to chlorite and epidote. Accessory minerals include magnetite, pyrite, ilmenite, apatite and zircon (Fig. 3e, f).

4. Analytical methods

4.1. Zircon geochronology and geochemistry

Zircon grains were separated from samples 16VN08–08–06 and 16VN08–09–06 by heavy–liquid and magnetic methods, then were mounted in epoxy resin before being polished to expose the interior of the crystals. Cathodoluminescence (CL) images were taken to examine zircon morphology, internal textures, and to guide spot selection during U–Pb analysis. U–Pb dating and trace element analyses were conducted by LA–ICP–MS at the State Key Laboratory of Geological Processes and Mineral Resources (GPMR), China University of Geosciences (Wuhan) (CUGW). Zircon standards GJ–1 and 91500 were used to monitor reproducibility, and instrument stability. During the analyses, the spot size of laser beam was 32 μm in diameter. Detailed analytical procedure is similar to that described by Liu et al. (2008, 2010). The off–line data calibration was conducted using the ICPMSDataCal program (Liu et al., 2008). Common–Pb correction followed the procedure of Andersen (2002). Concordia diagrams and weighted mean calculations were made using Isoplot/Ex_ver3 (Ludwig, 2003). Analytical results are listed in Tables 1, 2.

4.2. Zircon Lu–Hf isotope analysis

Zircon in–situ Hf isotopic data were collected on a Neptune Plus MC–ICP–MS (Thermo Fisher Scientific, Germany) in combination with a Geolas 2005 excimer ArF laser ablation system (Lambda Physik, Göttingen, Germany) at GPMR, CUGW. A laser beam of 44 μm in diameter was used. Helium was used as carrier gas in order to transport the ablated aerosols from the ablation cell to the ICP–MS torch. The instrumental conditions and detailed analytical procedures were similar to those described by Hu et al. (2012). The interference of ^{176}Yb and ^{176}Lu on ^{176}Hf was corrected by measuring the interference–free ^{173}Yb, ^{175}Lu isotopes and then using the known ratios ^{176}Yb/^{173}Yb = 0.79381 (Segal et al., 2003) and ^{176}Lu/^{175}Lu = 0.02656 (Blichert-Toft and Albarede, 1997) to calculate ^{176}Yb/^{177}Hf and ^{176}Lu/^{177}Hf, respectively. The ^{176}Lu decay constant of 1.865×10^{-11} a^{-1} (Scherer et al., 2001) was used for calculation of the initial Hf isotope values. The calculated model ages (T_{DM}) are based on the depleted mantle model suggested by Griffin et al. (2000). The analytical data are given in Table 3.

4.3. Plagioclase geochemistry

Plagioclase composition was determined by a JEOL JXA–8100 Electron Probe Micro Analyzer equipped with four wavelength–dispersive spectrometers (WDS) at the GPMR. Operating conditions were: 15 kV accelerating voltage, 20 nA beam current and a spot size of 10 μm. Data were corrected on–line using a modified ZAF (atomic number, absorption, fluorescence) correction procedure. The used standards were Sanidine (K, Al), Pyrope Garnet (Fe), Diopsode (Ca, Mg), Jadeite (Na), Rhodonite (Mn), Olivine (Si), Rutile (Ti). The analytical data are given in Table 4.

4.4. Whole–rock geochemistry

Eleven fresh samples selected for whole–rock geochemical analysis were powdered to finer than 200 mesh. Major and trace elements were analyzed by XRF–1800 spectrometry and by an Agilent 7500a ICP–MS, respectively, at the GPMR. Detailed sample digesting procedures and the analytical precision and accuracy for major and trace elements are described by Ma et al. (2012) and Liu et al. (2008), respectively. The analytical results are shown in Table 5.

Table 1
LA-ICP-MS zircon U–Pb data for the Dieng Bong plagiogranites.

Spot number	Th	U	Th/U	$^{207}Pb/^{206}Pb$		$^{207}Pb/^{235}U$		$^{206}Pb/^{238}U$		Error correlation	$^{207}Pb/^{206}Pb$		$^{207}Pb/^{235}U$		$^{206}Pb/^{238}U$		Concordance
	ppm			Ratio	±1σ	Ratio	±1σ	Ratio	±1σ		Age	±1σ	Age	±1σ	Age	±1σ	
Sample 16VN08-08-06																	
01	621	964	0.64	0.0568	0.0013	0.6998	0.0159	0.0889	0.0008	0.3790	487	48.1	539	9.5	549	4.5	98%
02	268	639	0.42	0.0580	0.0013	0.6647	0.0163	0.0827	0.0009	0.4477	532	54.6	517	9.9	512	5.4	98%
03	272	494	0.55	0.0546	0.0013	0.6140	0.0155	0.0812	0.0008	0.4098	398	53.7	486	9.8	503	5.0	96%
04	86.3	247	0.35	0.0574	0.0016	0.6330	0.0183	0.0798	0.0008	0.3467	506	61.1	498	11.4	495	4.8	99%
05	210	557	0.38	0.0570	0.0013	0.6409	0.0148	0.0813	0.0008	0.4240	500	50.0	503	9.1	504	4.7	99%
06	316	575	0.55	0.0561	0.0014	0.6272	0.0161	0.0808	0.0008	0.3875	457	55.6	494	10.1	501	4.8	98%
07	275	779	0.35	0.0578	0.0014	0.5670	0.0136	0.0709	0.0007	0.3823	520	47.2	456	8.8	442	3.9	96%
08	776	897	0.87	0.0559	0.0014	0.6164	0.0154	0.0795	0.0008	0.4141	450	53.7	488	9.7	493	4.9	98%
09	130	415	0.31	0.0565	0.0016	0.6266	0.0185	0.0803	0.0010	0.4214	472	97.2	494	11.5	498	6.0	99%
10	88.0	209	0.42	0.0563	0.0019	0.6833	0.0257	0.0876	0.0014	0.4332	465	76	529	15.5	542	8.5	97%
11	278	509	0.55	0.0565	0.0015	0.6213	0.0166	0.0796	0.0008	0.3832	472	59.3	491	10.4	494	4.9	99%
12	336	670	0.50	0.0551	0.0013	0.6202	0.0155	0.0811	0.0008	0.4068	417	56.5	490	9.7	503	4.9	97%
13	286	670	0.43	0.0579	0.0013	0.6416	0.0147	0.0800	0.0007	0.4065	528	50.0	503	9.1	496	4.5	98%
14	204	414	0.49	0.0553	0.0014	0.6121	0.0155	0.0802	0.0008	0.3904	433	57.4	485	9.8	497	4.7	97%
15	1010	1027	0.98	0.0578	0.0011	0.6717	0.0133	0.0839	0.0007	0.4156	524	42.6	522	8.1	519	4.1	99%
16	137	396	0.35	0.0577	0.0015	0.6419	0.0169	0.0803	0.0008	0.3605	517	55.6	503	10.5	498	4.6	98%
17	196	602	0.33	0.0599	0.0015	0.6668	0.0167	0.0804	0.0008	0.3926	598	51.8	519	10.2	499	4.7	96%
18	249	387	0.64	0.0563	0.0015	0.6512	0.0183	0.0838	0.0009	0.4000	465	28.7	509	11.2	519	5.6	98%
19	153	352	0.43	0.0591	0.0017	0.6705	0.0202	0.0818	0.0009	0.3543	572	63.0	521	12.3	507	5.2	97%
Sample 16VN08-09-06																	
01	150	300	0.50	0.0624	0.0016	0.7144	0.0191	0.0829	0.0010	0.4361	700	53.7	547	11.3	514	5.8	93%
02	181	371	0.49	0.0569	0.0015	0.6519	0.0176	0.0830	0.0008	0.3736	487	57.4	510	10.8	514	5.0	99%
03	153	321	0.48	0.0582	0.0016	0.6690	0.0195	0.0832	0.0009	0.3707	600	59.3	520	11.9	515	5.4	99%
04	39.6	130	0.31	0.0597	0.0021	0.6933	0.0245	0.0847	0.0010	0.3358	591	106	535	14.7	524	6.0	97%
05	195	358	0.54	0.0582	0.0014	0.6841	0.0172	0.0866	0.0027	1.2509	539	51.8	529	10.4	536	16.2	98%
06	237	432	0.55	0.0604	0.0013	0.6965	0.0156	0.0835	0.0007	0.3962	617	48.1	537	9.4	517	4.4	96%
07	65.3	175	0.37	0.0591	0.0019	0.7049	0.0234	0.0867	0.0011	0.3838	572	72.2	542	13.9	536	6.6	98%
08	82.7	248	0.33	0.0591	0.0017	0.7114	0.0209	0.0871	0.0009	0.3637	569	63.0	546	12.4	538	5.5	98%
09	73.1	209	0.35	0.0675	0.0063	0.7713	0.0667	0.0837	0.0010	0.1371	854	190	580	38.2	518	5.9	88%
10	80.4	221	0.36	0.0578	0.0021	0.6514	0.0229	0.0816	0.0009	0.3108	520	77.8	509	14.1	506	5.3	99%
11	342	530	0.65	0.0577	0.0015	0.6729	0.0178	0.0842	0.0010	0.4455	520	57.4	522	10.8	521	5.9	99%
12	105	265	0.39	0.0599	0.0020	0.6997	0.0228	0.0844	0.0010	0.3666	611	72.2	539	13.6	523	6.0	96%
13	58.2	191	0.31	0.0583	0.0020	0.6895	0.0236	0.0857	0.0010	0.3542	539	74.1	533	14.2	530	6.2	99%
14	47.3	131	0.36	0.0593	0.0024	0.6865	0.0273	0.0840	0.0010	0.3075	576	88.9	531	16.5	520	6.1	97%
15	101	252	0.40	0.0601	0.0019	0.7009	0.0225	0.0845	0.0009	0.3486	609	68.5	539	13.4	523	5.6	96%
16	33.6	118	0.28	0.0583	0.0022	0.6574	0.0242	0.0820	0.0010	0.3296	539	84.1	513	14.8	508	5.9	99%
17	84.9	196	0.43	0.0595	0.0021	0.6699	0.0230	0.0817	0.0009	0.3148	583	75.9	521	14.0	506	5.3	97%

5. Results

5.1. Zircon U–Pb dating, Lu–Hf isotopic composition and mineral geochemistry

Thirty–six analyses on 36 grains from samples 16VN08–08–06 and 16VN08–09–06 of the Dieng Bong Complex are listed in Table 1, and shown in Fig. 4a, b.

All zircon grains are transparent and colorless, subhedral to euhedral and 100–300 μm in length, with width/length ratios of about 1:1–1:3. Most zircon crystals from sample 16VN08–08–06 display broad sector zoning and low CL intensity (Fig. 4a). By contrast, zircon grains from sample 16VN08–09–06 are planar, show sector or oscillatory zoning and moderate to strong CL intensity (Fig. 4b). All spots record a wide range of U (118–1027 ppm) and Th (34–1010 ppm) concentrations, with Th/U ratios in the range of 0.28–0.98 (Table 1). Collectively, the Th/U ratios and CL image features indicate that all the zircon crystals have a magmatic origin.

Nineteen analyses were taken on 19 grains from sample 16VN08–08–06. Excluding three discordant analyses (01, 07, 10), the remaining 16 concordant ones yielded a weighted mean $^{206}Pb/^{238}U$ age of 502.1 ± 6.0 Ma (MSWD = 0.46) (Fig. 4c), which is interpreted as the crystallization age of the sample.

Seventeen zircon grains from sample 16VN08–09–06 were analyzed. All but one (spot 05, Table 1) are concordant, and yielded a weighted mean $^{206}Pb/^{238}U$ age of 518.5 ± 7.1 Ma (MSWD = 0.4) (Fig. 4d), interpreted as the crystallization age of the sample.

All zircon grains analyzed in this study have low U/Yb (due to their low U and high Yb) and high Hf values, thus most of them fall in the fields of ocean crust zircon defined by Grimes et al. (2007) (Fig. 5a, b, c). Other zircon geochemical diagrams (Fig. 5d, e, f) show negative correlations between Nb, U/Yb with Hf, Gd/Yb, respectively, and positive correlation between Gd/Yb and Ce/Yb.

Hf isotope analyses were made on 25 zircon grains from samples 16VN08–08–06 and 16VN08–09–06 (Table 3, Fig. 4a, b). The initial εHf values range from +11 to +16 (average of +14) and from +13 to +16 (average of +15) for the 16VN08–08–06 and 16VN08–09–06, respectively (Table 3, Fig. 5g).

Plagioclase compositions from samples 16VN08–08–06 and 16VN08–09–06 show low K_2O (0.04–0.19%), CaO (2.69–5.62%) and high Na_2O (8.40–10.24%) plotting within the oligoclase field on the Ab–Or–An ternary diagram of Deer et al. (1992) with An from 20 to 28 for the 16VN08–08–06 and 13 to 24 for the 16VN08–09–06 (Table 4, Fig. 5h).

5.2. Whole–rock major and trace element geochemistry

The loss on ignition (LOI) values of all samples are relatively low (0.44–0.9 wt%) (Table 5), and display no correlations with major oxides and fluid–mobile elements (e.g., Rb and K, not shown), suggesting that effects of alteration and/or metamorphism are negligible.

Based on the CIPW norms calculated from the major element compositions, all the 16VN08–09 samples (16VN08–09–01, –02, –03, –04, –05, –06) are classified as trondhjemites, whereas the 16VN08–08

Table 2
Zircon trace elements analytical data for Dieng Bong plagiogranites.

Sam.	Spot	Nb	La	Ce	Pr	Nd	Sm	Eu	Gd	Tb	Dy	Ho	Er	Tm	Yb	Lu	U	U/Yb	Ce/Yb	Gd/Yb	Nb/Yb
16VN08-08-06	01	14	0.00	68	0.15	4	15	1	119	49	680	301	1531	362	3452	660	958	0.28	0.02	0.03	0.0041
	02	2	0.01	24	0.32	6	16	2	115	44	590	251	1272	300	2974	581	638	0.21	0.01	0.04	0.0008
	03	3	0.04	40	0.52	12	28	3	192	72	924	375	1747	403	3715	701	497	0.13	0.01	0.05	0.0009
	04	3	0.19	16	0.36	4	10	1	89	35	476	195	915	194	1892	355	245	0.13	0.01	0.05	0.0018
	05	1	0.00	12	0.07	1	4	1	33	14	214	102	572	147	1680	349	556	0.33	0.01	0.02	0.0009
	06	9	0.09	35	0.27	4	16	2	147	58	764	311	1431	311	2892	542	575	0.20	0.01	0.05	0.0031
	07	3	0.03	24	0.28	5	14	1	101	40	539	234	1207	286	3020	604	715	0.24	0.01	0.03	0.0011
	08	11	0.03	64	0.42	9	27	3	202	75	986	404	1844	424	3861	709	887	0.23	0.02	0.05	0.0028
	09	3	0.01	14	0.09	3	9	1	78	32	448	197	988	230	2402	477	430	0.18	0.01	0.03	0.0011
	10	2	0.56	12	0.22	2	4	0	40	16	223	93	445	98	977	183	197	0.20	0.01	0.04	0.0024
	11	4	0.02	47	0.63	14	39	3	278	103	1305	513	2169	485	4190	759	511	0.12	0.01	0.07	0.0010
	12	4	0.03	37	0.41	8	21	2	137	53	722	312	1608	379	3693	720	670	0.18	0.01	0.04	0.0012
	13	5	0.02	27	0.16	3	11	1	93	38	549	250	1315	317	3199	641	670	0.21	0.01	0.03	0.0014
	14	3	0.02	29	0.49	9	26	3	179	66	851	345	1636	368	3401	642	415	0.12	0.01	0.05	0.0009
	15	12	0.01	56	0.29	8	27	3	203	73	917	360	1643	348	3208	597	1002	0.31	0.02	0.06	0.0037
	16	1	0.03	8	0.10	2	4	1	29	12	171	77	431	111	1281	271	361	0.28	0.01	0.02	0.0007
	17	2	0.01	15	0.18	4	9	2	72	28	388	169	889	214	2295	465	601	0.26	0.01	0.03	0.0007
	18	5	0.47	23	0.42	5	15	2	128	50	642	253	1124	230	2144	387	401	0.19	0.01	0.06	0.0024
	19	2	0.02	21	0.31	6	16	2	124	47	623	258	1252	279	2769	522	360	0.13	0.01	0.04	0.0008
16VN08-09-06	01	11	0.01	52	0.36	11	39	5	366	141	1891	740	3447	688	6806	1170	862	0.13	0.01	0.05	0.0016
	02	16	0.57	60	0.61	9	30	4	296	117	1591	631	2995	605	6095	1059	1057	0.17	0.01	0.05	0.0026
	03	12	0.03	48	0.37	9	33	4	319	125	1704	669	3127	631	6267	1094	899	0.14	0.01	0.05	0.0018
	04	4	0.00	15	0.09	3	14	2	141	58	851	355	1740	365	3767	682	364	0.10	0.00	0.04	0.0010
	05	13	0.01	49	0.17	5	22	3	246	98	1363	545	2568	531	5370	948	1004	0.19	0.01	0.05	0.0024
	06	18	0.01	82	0.62	16	60	7	523	198	2630	1007	4607	927	8716	1549	1189	0.14	0.01	0.06	0.0020
	07	5	23.51	109	16.45	115	63	5	286	97	1305	512	2401	487	4873	863	490	0.10	0.02	0.06	0.0011
	08	9	0.00	30	0.20	4	22	3	223	91	1313	549	2714	566	5895	1068	715	0.12	0.01	0.04	0.0015
	09	7	0.01	33	0.27	7	28	3	249	100	1409	571	2772	573	5771	1023	576	0.10	0.01	0.04	0.0012
	10	8	0.02	38	0.12	5	20	3	209	85	1186	480	2313	483	4915	871	635	0.13	0.01	0.04	0.0016
	11	24	0.02	93	0.37	11	45	6	449	171	2317	898	4184	848	8389	1454	1508	0.18	0.01	0.05	0.0028
	12	11	0.00	40	0.11	4	18	3	191	78	1118	453	2189	456	4651	833	761	0.16	0.01	0.04	0.0023
	13	7	0.02	29	0.11	3	13	2	142	60	858	355	1755	371	3876	705	553	0.14	0.01	0.04	0.0019
	14	4	1.79	24	1.40	13	23	3	195	76	1064	426	2014	410	4128	733	367	0.09	0.01	0.05	0.0009
	15	7	0.01	47	0.58	14	47	5	403	153	2075	817	3818	773	7739	1340	710	0.09	0.01	0.05	0.0008
	16	4	0.23	17	0.20	3	11	2	120	50	723	297	1448	303	3143	567	328	0.10	0.01	0.04	0.0013
	17	6	0.00	26	0.09	2	14	2	141	56	827	337	1628	334	3416	612	555	0.16	0.01	0.04	0.0018

Table 3
Zircon in-situ Lu–Hf isotopic compositions of Dieng Bong plagiogranites.

Spot no.	$^{176}Hf/^{177}Hf$	1σ	$^{176}Lu/^{177}Hf$	1σ	$^{176}Yb/^{177}Hf$	1σ	Age (Ma)	$(^{176}Hf/^{177}Hf)_i$	εHf(0)	1σ	εHf(t)	1σ	TDM1	TDM2	fLu/Hf
Sample 16VN08-08-06															
01	0.282921	0.000032	0.008089	0.000041	0.400875	0.007583	549	0.282838	5	1.23	14	1.26	579	589	−0.76
02	0.282987	0.000060	0.010918	0.000072	0.543825	0.014836	512	0.282882	8	2.18	15	2.21	511	511	−0.67
03	0.282960	0.000042	0.010969	0.000052	0.558199	0.011319	503	0.282856	7	1.57	14	1.60	563	565	−0.67
04	0.282960	0.000048	0.006280	0.000058	0.336710	0.010062	495	0.282902	7	1.78	16	1.81	481	478	−0.81
05	0.282887	0.000023	0.005213	0.000062	0.242388	0.004342	504	0.282838	4	0.97	13	1.01	583	604	−0.84
09	0.282995	0.000043	0.009213	0.000090	0.489290	0.008444	498	0.282909	8	1.61	16	1.65	466	463	−0.72
11	0.282973	0.000045	0.009800	0.000153	0.529858	0.010947	494	0.282882	7	1.68	15	1.74	516	517	−0.70
12	0.282879	0.000047	0.009750	0.000081	0.488431	0.011146	503	0.282787	4	1.73	12	1.77	690	703	−0.71
14	0.282997	0.000056	0.009957	0.000087	0.511592	0.011027	497	0.282904	8	2.06	16	2.10	474	473	−0.70
15	0.282929	0.000049	0.009752	0.000062	0.532964	0.011711	519	0.282834	6	1.82	13	1.86	597	604	−0.71
17	0.282932	0.000039	0.008661	0.000133	0.407692	0.005113	499	0.282851	6	1.47	14	1.53	570	578	−0.74
18	0.282868	0.000029	0.006402	0.000038	0.341747	0.009193	519	0.282806	3	1.16	12	1.19	636	663	−0.81
19	0.282841	0.000047	0.007194	0.000155	0.375287	0.013670	507	0.282773	2	1.73	11	1.79	698	731	−0.78
Ave.											14				
Sample 16VN08-09-06															
01	0.282932	0.000019	0.004402	0.000106	0.215271	0.002796	514	0.282889	6	0.84	16	0.89	499	494	−0.87
02	0.282919	0.000032	0.006053	0.000074	0.281343	0.006828	514	0.282860	5	1.26	15	1.30	546	552	−0.82
03	0.282867	0.000023	0.004638	0.000061	0.201478	0.001301	515	0.282822	3	0.97	13	1.01	604	626	−0.86
06	0.282888	0.000033	0.004924	0.000031	0.255549	0.004807	517	0.282841	4	1.26	14	1.29	575	590	−0.85
09	0.282901	0.000028	0.004104	0.000069	0.217586	0.001911	518	0.282861	5	1.13	15	1.16	542	549	−0.88
11	0.282925	0.000043	0.007731	0.000070	0.400098	0.005532	521	0.282849	5	1.62	14	1.65	565	571	−0.77
12	0.282943	0.000029	0.004748	0.000024	0.251864	0.005304	523	0.282897	6	1.15	16	1.18	486	478	−0.86
13	0.282941	0.000029	0.005058	0.000035	0.258033	0.005794	530	0.282890	6	1.14	16	1.17	495	489	−0.85
14	0.282879	0.000030	0.003051	0.000070	0.155528	0.003448	520	0.282849	4	1.16	14	1.20	560	573	−0.91
15	0.282918	0.000036	0.005544	0.000060	0.290571	0.008186	523	0.282864	5	1.38	15	1.42	538	543	−0.83
16	0.282906	0.000028	0.003567	0.000095	0.177654	0.002528	508	0.282872	5	1.10	15	1.15	527	530	−0.89
17	0.282910	0.000025	0.003072	0.000058	0.158112	0.001535	506	0.282881	5	1.01	15	1.05	513	511	−0.91
Ave.											15				

Table 4
Electron microprobe analyses of plagioclase in the Dieng Bong plagiogranites.

Sample	16VN08-08-06						16VN08-09-06					
Spot	01	02	03	04	05	06	01	02	03	04	05	06
Na_2O	9.53	9.09	9.12	8.84	8.40	8.99	9.31	8.69	8.71	8.74	9.36	10.24
K_2O	0.08	0.04	0.05	0.04	0.06	0.07	0.19	0.66	0.15	0.13	0.07	0.09
FeO	0.03	0.03	0.04	0.08	0.04	0.06	0.02	0.04	0.06	0.07	0.03	0.05
MgO	-	-	0.01	0.01	-	0.00	0.01	0.01	0.01	0.01	-	0.00
CaO	3.98	4.71	4.37	4.81	5.62	4.83	3.51	4.27	4.82	5.25	4.52	2.69
MnO	-	0.03	-	-	0.03	0.04	-	0.02	-	-	0.01	0.00
Al_2O_3	22.98	23.29	22.98	23.34	24.30	23.36	21.82	23.05	23.49	23.42	23.02	21.75
TiO_2	-	0.00	-	0.01	0.01	-	-	-	0.00	0.01	-	-
SiO_2	64.05	63.61	63.74	62.59	62.01	63.11	64.07	63.19	62.77	62.13	63.07	66.09
Total	100.66	100.79	100.30	99.71	100.45	100.45	98.94	99.92	100.00	99.77	100.08	100.91
Or	0	0	0	0	0	0	1	4	1	1	0	1
Ab	80	76	77	75	71	76	80	74	74	74	77	86
An	20	23	22	24	28	23	17	21	24	24	21	13

"-" below limit of detection.

samples (16VN08–08–01, –02, –03, –05, –06) are transitional between tonalites and trondhjemites in the An–Ab–Or diagram (Barker, 1979) (Fig. 6a). They show high SiO_2 (63.6–74.9) and Na_2O (4.2–5.8 wt%) (Table 5). Fig. 6b shows that the 16VN08–08 samples belong to dacitic rocks, while most of the 16VN08–09 samples plot in the rhyolitic field. Overall, most samples are calcic, and follow a trend roughly parallel to the boundary between the calcic and calc–alkalic fields in the modified alkali–lime index (MALI) diagram (Fig. 6c). The exceptions include three samples (16vn08–08–02, 16vn08–08–05, and 16vn08–08–06), which straddle the boundary, likely due to their high modal plagioclase (Frost and Frost, 2008), as also evidenced by their elevated Sr values compared to other 16vn08–08 samples (Table 5). Frost et al. (2001) and Frost and Frost (2008) noticed that the boundary between tholeiitic and calc–alkaline fields proposed by Miyashiro (1974) was only applicable to rocks with >60% SiO_2, but not to those having SiO_2 < 60%. Therefore, they suggested a Fe–index diagram to distinguish Fe–enriched (ferroan) melts from Mg–enriched (magnesian) ones. All our studied samples are magnesian according to this classification (Fig. 6d). In Fig. 6e, all samples define an evolutionary trend characteristic of calc–alkaline suites (Irvine and Baragar, 1971).

All samples show low contents of Al_2O_3 (12.9–16.1 wt%) and K_2O (0.38–0.52 wt%) (Table 5). The aluminum–saturation index versus silica plot (Frost and Frost, 2008) shows that these samples are scattered around the boundary between the metaluminous and peraluminous fields (Fig. 6f). Fig. 6g confirms that all but one (16vn08–09–03) of the samples plot within the field of the aluminum–poor trondhjemites of Barker (1979), whereas Fig. 6h shows that all samples fall in the low K_2O field defined by Coleman and Donato (1979). There are general decreases in Al_2O_3, MgO, FeO, TiO_2, CaO and a slight increase in K_2O with increasing SiO_2 (Figs. 6g, h, 7a, b, c, d).

Fig. 7e, f shows inverse correlation between Sr and Rb, but positive correlation between Ba and K. Nickel and Cr values are generally high with no (or inverse) correlation to MgO content (Fig. 7g, h), likely indicating the cumulation of sulfide phases (Pearce et al., 1995). This is in agreement with petrographic observations of abundant pyrite.

These rocks have low Sr (74–175 ppm) and high Y (20–48 ppm) concentrations (Table 5). In the Sr/Y vs. Y diagram (Fig. 8a), none of the studied samples lie within the high Sr/Y "adakite" field defined by Defant and Drummond (1990). The rare earth elements (REEs) are relatively low with total REEs ranging from 35 to 58 ppm in the 16vn08–08 sample and 26 to 34 ppm in the 16vn08–09 sample (Table 5). In a chondrite–normalized REE diagram, all samples are characterized by depletions of LREEs relative to HREEs (La/Yb_N = 0.37–0.76) with distinctive but variable Eu anomalies (Eu/Eu^* = 0.50–1.43) (Table 5, Fig. 8b). In the N–MORB normalized multi–element diagrams, all the samples show coherent patterns, with high LILEs (e.g. Cs, Rb, Ba, Pb, K), Th, U and low HFSEs (e.g., Nb and Ti) (Fig. 8c). The slightly positive Zr and Hf anomalies might be attributed to accumulation of zircon. Selected tectonic discrimination diagrams (Fig. 8d, e, f, g) show that the studied rocks are closely analogous to those of the Troodos (Freund et al., 2014) and Talkeetna (Kelemen et al., 2014) intra–oceanic arcs.

6. Discussion

6.1. Rock classification

Trondhjemite–tonalite–diorite suite is characterized by mineral assemblages dominated by plagioclase, quartz, with minor, variable amounts of hornblende, biotite and/or pyroxene, and is compositionally calcic and magnesian. They are important constituents of Archean gneiss terrains, where they form so–called continental trondhjemites. Moreover, they are also a component of oceanic arc and mid ocean ridge associations, where they are named oceanic plagiogranites (e.g., Coleman and Donato, 1979; Le Maitre, 1989; Koepke et al., 2007; Zi et al., 2012; Frost et al., 2016). Continental trondhjemites bear some geochemical characteristics similar to adakites, e.g., high in Al, Sr, low in Y, HREE and enriched in LREE. On the contrary, oceanic plagiogranites are featured by low Al, K, Sr, Rb and high Y (Martin et al., 2005; Frost et al., 2016).

Samples from the Dieng Bong Complex in the present study share many similarities with trondhjemites/plagiogranites in both mineral assemblage (i.e., mainly consist of plagioclase, quartz, with minor amounts of hornblende and biotite) and chemical composition (i.e., calcic and magnesian). Moreover, SiO_2 contents and the An–Ab–Or ternary diagram support classification of the 16VN08–08 and 16VN08–09 samples as tonalites (dacitic) and trondhjemites (rhyolitic), respectively. On the other hand, the samples are characterized by high modal plagioclase and quartz, high Y, low Al_2O_3, K_2O, Sr, Rb contents, and depletion in LREE with flat HREE patterns, similar to typical oceanic plagiogranites.

6.2. Petrogenesis

The petrogenesis of trondhjemite–tonalite–diorite suites is extremely complicated, and has been a subject of much debate (e.g., Koepke et al., 2007; Frost et al., 2016, for review). Such silicic magmas can be formed in different tectonic settings through differing processes (e.g., Brophy, 2008, 2009). As the studied plagiogranites were formed in intra–oceanic arc settings (see below), two possible processes have been invoked to explain the generation of silicic magmas in such settings, i.e., extensive fractional crystallization of hydrous basaltic magma, and dehydration melting of lower crustal amphibolites (e.g., Pu et al., 2014; Haase et al., 2016). However, distinguishing the two processes from one another is not straightforward since both fractionation and dehydration melting can lead to similar major, trace

Table 5
Major and trace elements analytical data for Dieng Bong plagiogranites.

Samples	16VN08-08-					16VN08-09-					
	-01	-02	-03	-05	-06	-01	-02	-03	-04	-05	-06
SiO_2	70.39	64.42	70.81	63.55	63.68	74.88	74.71	69.51	74.04	73.7	74.38
Al_2O_3	13.93	15.32	13.86	15.24	15.26	13.29	12.91	16.1	13.71	13.81	13.02
FeOT	4.08	6.40	3.89	6.60	6.57	1.67	2.38	2.23	1.89	1.94	2.88
FeO	3.46	5.44	3.30	5.61	5.58	1.42	2.03	1.90	1.61	1.65	2.45
MgO	1.33	2.65	1.41	2.72	2.75	0.77	0.86	0.65	0.87	0.83	0.84
CaO	3.5	3.59	2.96	3.92	4.02	1.93	2.21	3.6	2.22	1.92	2.6
Na_2O	4.48	5.11	4.45	5.27	5.25	5.4	4.85	5.81	5.12	5.61	4.2
K_2O	0.51	0.39	0.51	0.39	0.38	0.52	0.51	0.38	0.52	0.5	0.52
TiO_2	0.41	0.58	0.4	0.58	0.59	0.35	0.31	0.38	0.34	0.34	0.35
P_2O_5	0.1	0.086	0.073	0.081	0.081	0.062	0.051	0.055	0.057	0.057	0.057
MnO	0.059	0.085	0.05	0.089	0.091	0.022	0.025	0.041	0.025	0.022	0.033
H2O-	0.08	0.12	0.04	0.04	0.02	0	0.02	0.1	0	0.08	0.1
LOI	0.44	0.82	0.64	0.74	0.6	0.72	0.74	0.9	0.68	0.86	0.64
Li	6.57	12.88	10.55	14.36	13.77	7.32	8.58	3.39	9.83	8.59	8.21
Be	0.35	0.36	0.53	0.36	0.34	0.42	0.35	0.49	0.43	0.44	0.34
Sc	24.20	31.15	20.68	25.85	25.70	12.29	15.31	13.52	14.68	13.94	7.88
V	56.78	105.30	56.02	121.87	122.24	36.73	31.11	35.66	39.18	41.26	25.59
Cr	2.82	1.76	3.20	1.98	1.83	3.42	2.76	2.47	2.65	3.65	3.61
Co	205.21	142.48	256.44	154.92	133.72	260.31	227.21	206.90	207.90	283.00	297.01
Ni	109.94	73.36	137.14	79.66	66.17	137.74	119.66	103.54	112.89	157.14	161.51
Cu	8.06	2.31	11.37	2.49	2.11	3.05	5.37	9.07	2.67	3.61	20.97
Zn	22.08	34.57	21.39	32.91	32.28	11.94	12.14	9.89	12.05	13.53	13.00
Ga	14.04	15.69	13.81	15.98	15.80	12.48	12.15	12.50	12.98	12.78	12.98
Rb	5.01	4.48	4.95	4.42	4.36	5.99	5.71	3.99	6.45	5.79	4.90
Sr	142.25	163.07	125.94	173.60	175.29	73.85	117.06	113.76	84.81	76.54	105.19
Y	46.52	48.36	37.40	24.25	24.60	20.06	30.74	25.90	21.78	22.37	24.29
Zr	74.68	53.00	271.95	70.26	68.87	67.16	121.30	138.04	68.86	80.50	185.00
Nb	1.74	1.83	1.47	1.19	1.16	1.53	1.71	1.50	1.82	1.49	1.56
Mo	1.69	0.55	1.06	0.71	0.39	7.83	1.16	4.34	5.78	4.60	0.97
Cd	0.02	0.02	0.05	0.02	0.02	0.01	0.03	0.03	0.01	0.02	0.03
Sn	0.71	0.99	0.61	1.62	1.71	1.79	1.68	1.79	1.87	1.68	0.63
Cs	0.81	1.00	1.25	2.25	2.09	0.77	1.11	0.72	1.48	1.16	0.76
Ba	86.35	43.23	108.66	60.58	56.91	166.06	113.22	111.65	185.24	195.56	158.43
La	3.10	2.94	2.89	2.90	2.85	1.91	1.89	2.24	1.88	1.89	2.26
Ce	9.55	9.43	8.26	7.92	7.79	5.13	5.38	5.97	5.17	5.37	5.24
Pr	1.54	1.56	1.22	1.06	1.05	0.79	0.84	0.92	0.75	0.83	0.71
Nd	9.10	9.30	7.19	5.81	5.52	4.49	5.40	5.05	4.54	4.63	3.69
Sm	3.94	3.96	2.84	2.00	2.09	1.61	2.29	1.86	1.78	1.87	1.16
Eu	0.79	0.81	0.73	0.67	0.67	0.69	0.66	0.83	0.65	0.65	0.71
Gd	5.84	5.84	4.24	3.02	2.94	2.35	3.56	2.70	2.61	2.65	2.00
Tb	1.14	1.22	0.82	0.57	0.59	0.46	0.73	0.57	0.48	0.53	0.42
Dy	7.25	8.11	5.35	3.65	3.82	3.00	4.65	3.69	3.27	3.31	2.93
Ho	1.64	1.89	1.26	0.84	0.87	0.68	1.08	0.88	0.74	0.75	0.75
Er	4.86	5.50	3.92	2.56	2.60	2.03	3.16	2.70	2.21	2.17	2.39
Tm	0.74	0.84	0.65	0.42	0.42	0.31	0.53	0.43	0.35	0.36	0.41
Yb	4.75	5.63	4.35	2.73	2.82	2.08	3.61	3.06	2.41	2.39	2.87
Lu	0.72	0.82	0.72	0.44	0.47	0.33	0.56	0.52	0.37	0.37	0.49
Hf	2.54	2.24	7.78	2.38	2.28	2.55	3.81	4.51	2.63	2.90	5.25
Ta	2.41	1.51	1.95	1.71	1.44	1.85	2.50	2.20	2.45	1.94	2.33
Tl	0.05	0.04	0.04	0.05	0.06	0.06	0.05	0.04	0.05	0.05	0.03
Pb	1.04	1.11	0.98	1.11	1.12	1.14	1.31	1.54	1.39	1.32	0.71
Th	0.48	0.45	0.65	0.40	0.43	0.63	0.70	0.88	0.73	0.71	0.83
U	0.29	0.32	0.65	0.25	0.25	0.31	0.37	0.44	0.32	0.36	0.43
Or	3.07	2.36	3.08	2.36	2.30	3.11	3.06	2.28	3.12	3.00	3.12
Ab	38.61	44.27	38.49	45.76	45.47	46.32	41.68	49.95	43.98	48.22	36.10
An	16.70	17.66	14.52	17.21	17.35	9.29	10.80	17.00	10.80	9.30	12.72
Fe-index	0.72	0.67	0.70	0.67	0.67	0.65	0.70	0.74	0.65	0.67	0.74
MALI	1.49	1.91	2.00	1.74	1.61	3.99	3.15	2.59	3.42	4.19	2.12
ASI	0.98	1.00	1.05	0.95	0.94	1.03	1.03	0.98	1.06	1.05	1.07
∑REE	55	58	44	35	34	26	34	31	27	28	26
Eu/Eu^*	0.50	0.51	0.65	0.83	0.82	1.08	0.71	1.13	0.92	0.89	1.43
La/Yb_N	0.47	0.37	0.48	0.76	0.73	0.66	0.38	0.52	0.56	0.57	0.56
Th/Nb	0.27	0.25	0.44	0.34	0.37	0.41	0.41	0.59	0.40	0.48	0.53
La/Nb	1.78	1.60	1.97	2.44	2.46	1.25	1.11	1.49	1.03	1.27	1.44
Ba/La	27.81	14.73	37.60	20.86	19.94	86.82	59.97	49.94	98.42	103.29	70.20
Pb/Ce	0.11	0.12	0.12	0.14	0.14	0.22	0.24	0.26	0.27	0.24	0.14
Sr/Nd	15.63	17.54	17.52	29.89	31.76	16.44	21.68	22.54	18.70	16.51	28.52

Or, Ab, An calculated from CIPW norms; Fe-index = FeO / (FeO + MgO); MALI = $Na_2O + K_2O$-CaO; ASI = Al / (Ca − 1.67 * P + Na + K); $Eu/Eu^* = Eu / SQRT(Sm * Gd)_N$.

elements and isotopic characteristics in felsic magmas (Brophy, 2008). For the Dieng Bong plagiogranites, however, we suggest a petrogenetic model dominated by fractional crystallization based on evidences presented below: (1) The present plagiogranites occur as large (ca. 5 km^2), lenticular–shaped bodies with magmatic textures (Figs. 2a, c, 3a, b). These features are typically seen in plagiogranites of fractional crystallization origin (e.g., Freund et al., 2014; Haase et al., 2016), but are distinct from those formed by partial melting processes (Sawyer,

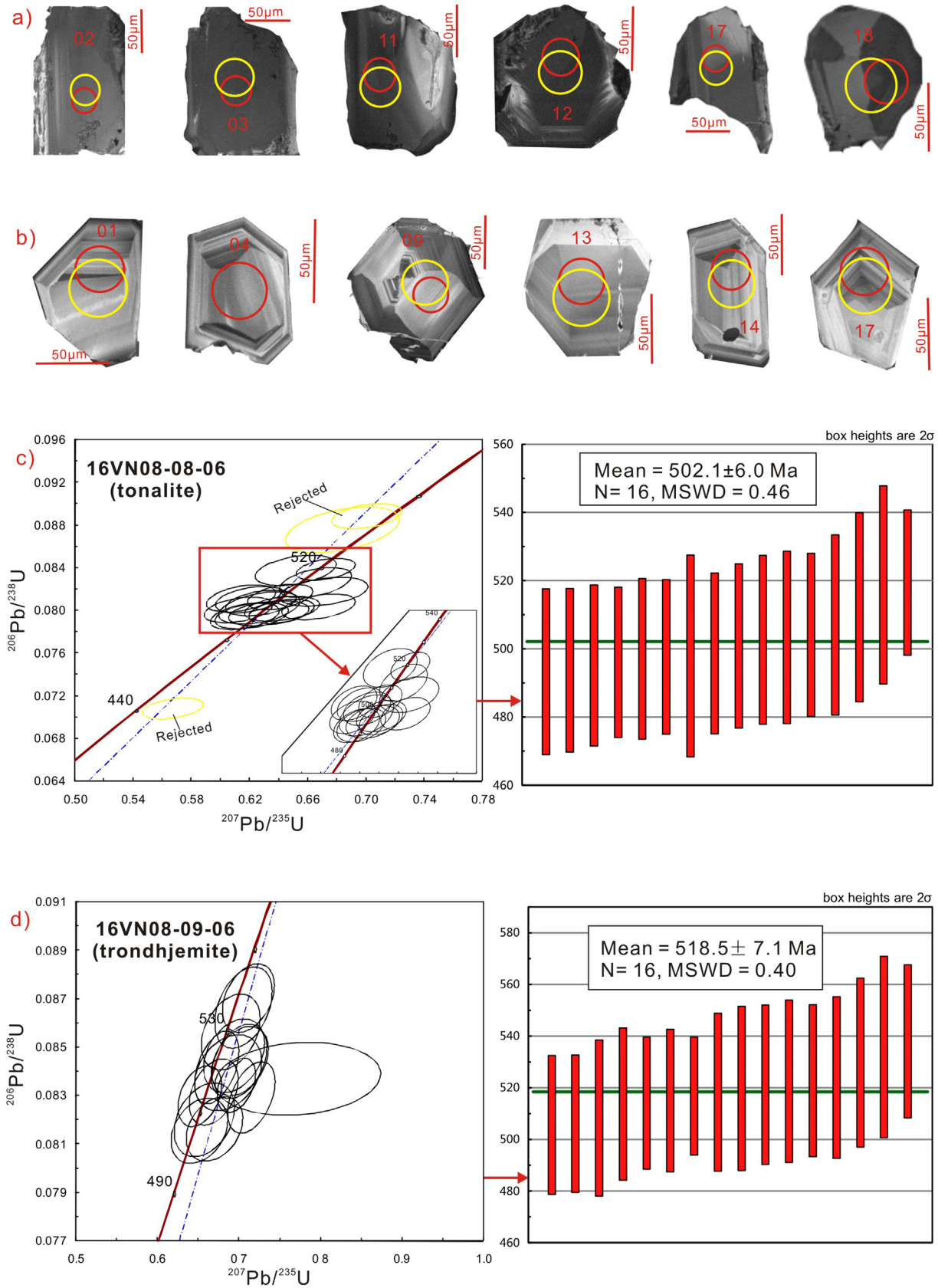

Fig. 4. Cathodoluminescence images showing morphology of represented zircon extracted from (a) 16VN08–08–06 and (b) 16VN08–09–06 samples. Red and yellow circles indicate the analytical sites for U–Pb and Hf isotopes, respectively. LA–ICP–MS zircon U–Pb concordia diagrams for (c) 16VN08–08–06 and (d) 16VN08–09–06 samples. (For interpretation of the references to color in this figure legend, the reader is referred to the web version of this article.)

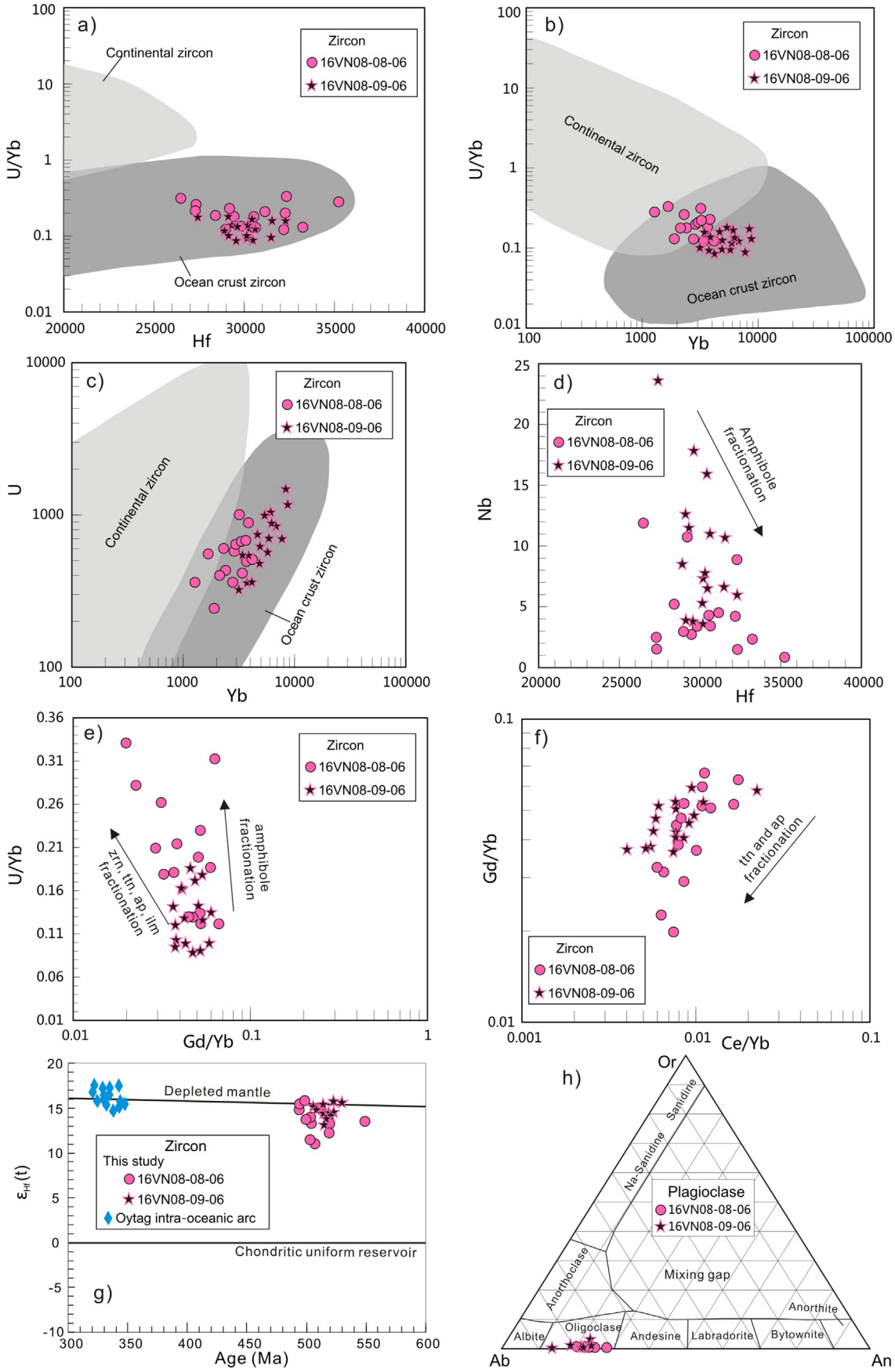

Fig. 5. Zircon geochemical diagrams for 16VN08–08–06 and 16VN08–09–06 samples: (a, b, c) U/Yb vs. Hf, U/Yb vs. Yb and U vs. Y discrimination diagrams (after Grimes et al., 2007); (d) Nb vs. Hf diagram (after Pietranik et al., 2017); (e, f) U/Yb vs. Gd/Yb and Gd/Yb vs. Ce/Yb diagrams (after Grimes et al., 2015). (g) Zircon $\varepsilon_{Hf}(t)$ vs. U–Pb ages diagram, Oytag intra-oceanic arc data of Jiang et al. (2008). (h) Feldspar (anorthite–albite–orthoclase) composition diagram for 16VN08–08–06 and 16VN08–09–06 samples (after Deer et al., 1992). Zrn–zircon, ttn–titanite, ap–apatite, ilm–ilmenite.

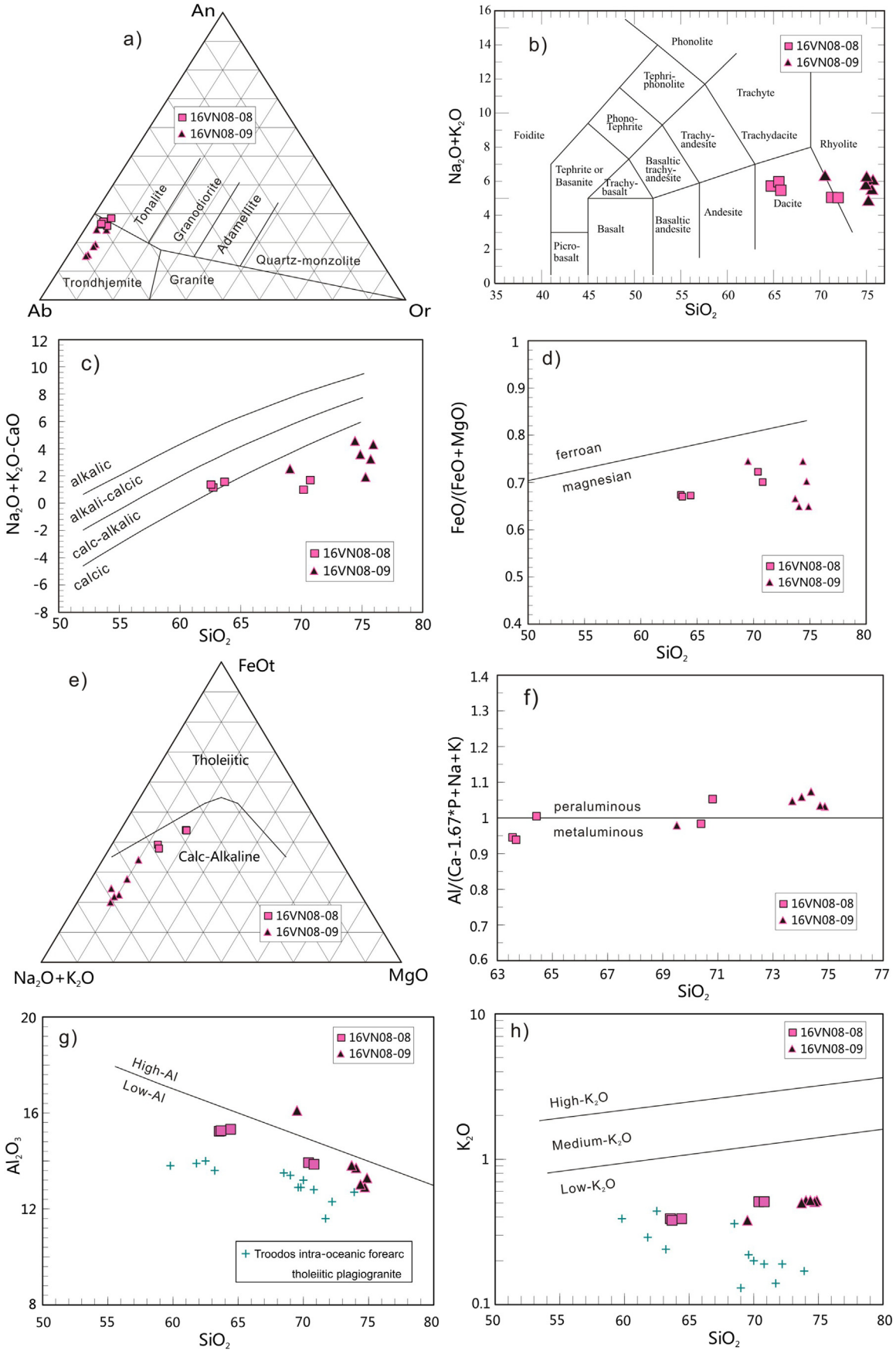

Fig. 6. Geochemical discrimination diagrams for 16VN08–08 and 16VN08–09 samples: (a) CIPW norms calculated from major element compositions of the rocks using the scheme suggested by Barker (1979); (b) total alkali–silica diagram (after Lebas et al., 1986); (c) modified alkali–lime index (MALI) diagram (after Frost et al., 2001); (d) Fe–index diagram (after Frost and Frost, 2008); (e) AFM diagram (after Irvine and Baragar, 1971); (f) aluminum–saturation index diagrams (after Frost and Frost, 2008); Al– (g) and K–boundary lines (h) are from Barker (1979) and Coleman and Donato (1979), respectively.

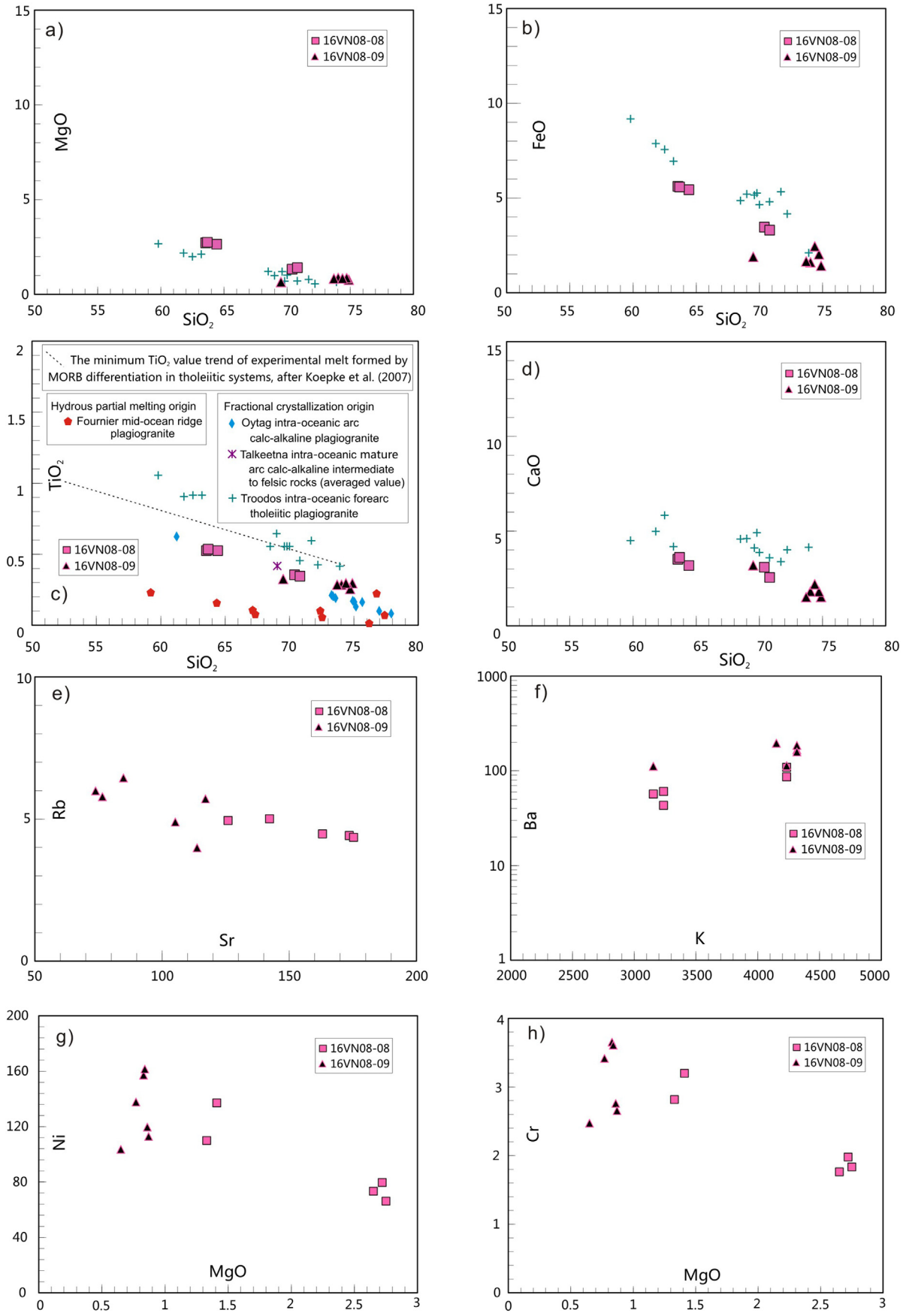

Fig. 7. Diagrams showing variation of SiO_2 with selected elements (a) MgO; (b) FeO; (c) TiO_2 and (d) CaO. Note that all our samples display similar trends with the Troodos fractionation–origin, intra–oceanic forearc tholeiitic plagiogranite data from Freund et al. (2014). (e) Inverse correlation between Sr and Rb by fractionation of plagioclase and biotite (e.g., Halliday et al., 1991; Frost et al., 2016); (f) increased Ba with K by fractionation of plagioclase (Perfit et al., 1980); (g, h) relatively high Ni, Cr contents and no (or inverse) correlation with MgO by accumulation of sulfide phases (Pearce et al., 1995).

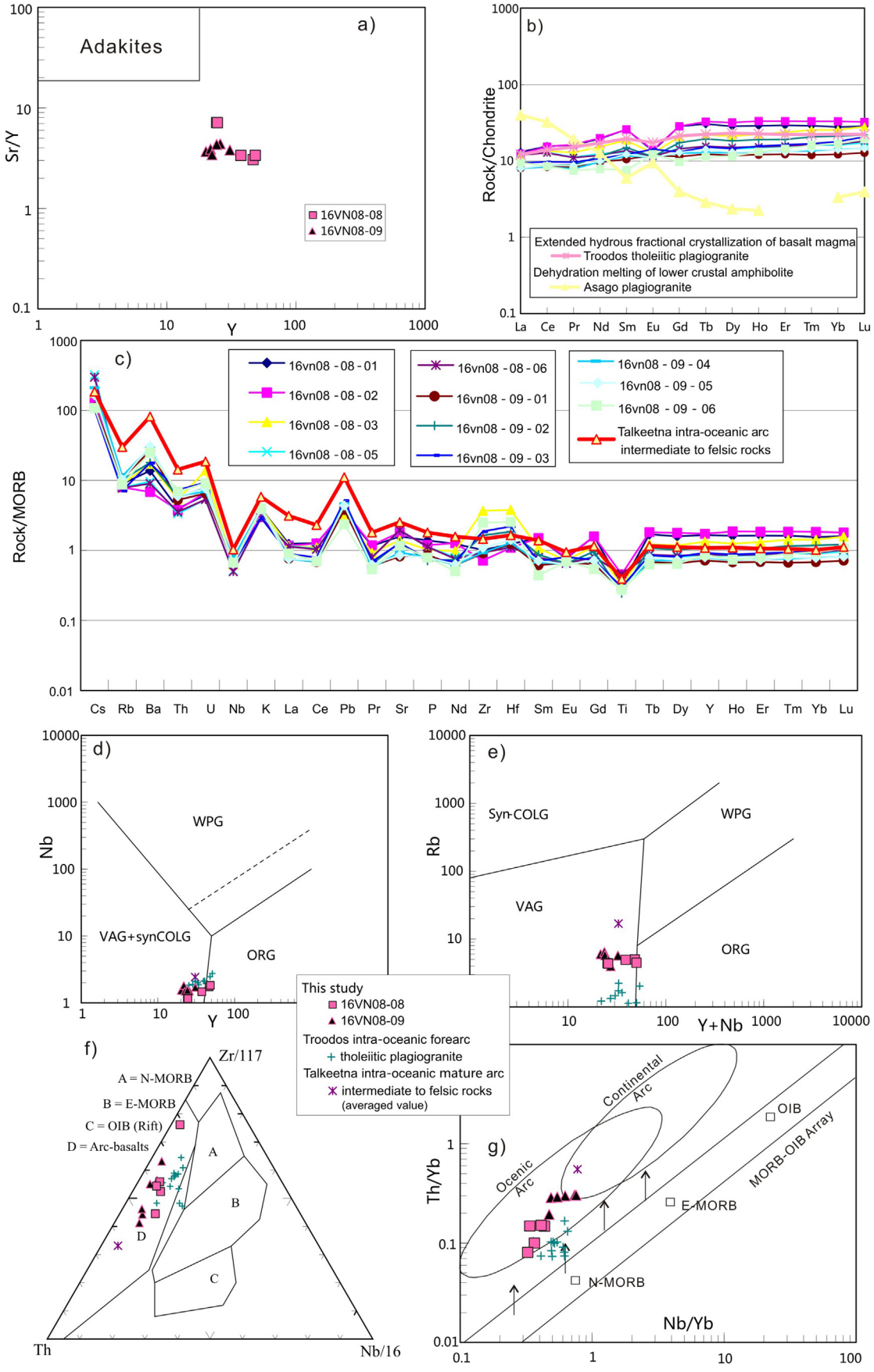
a)
Adakites
Sr/Y
Y
16VN08-08
16VN08-09
b)
Rock/Chondrite
Extended hydrous fractional crystallization of basalt magma
Troodos tholeiitic plagiogranite
Dehydration melting of lower crustal amphibolite
Asago plagiogranite
La Ce Pr Nd Sm Eu Gd Tb Dy Ho Er Tm Yb Lu
c)
Rock/MORB
16vn08 - 08 - 01
16vn08 - 08 - 02
16vn08 - 08 - 03
16vn08 - 08 - 05
16vn08 - 08 - 06
16vn08 - 09 - 01
16vn08 - 09 - 02
16vn08 - 09 - 03
16vn08 - 09 - 04
16vn08 - 09 - 05
16vn08 - 09 - 06
Talkeetna intra-oceanic arc
intermediate to felsic rocks
Cs Rb Ba Th U Nb K La Ce Pb Pr Sr P Nd Zr Hf Sm Eu Gd Ti Tb Dy Y Ho Er Tm Yb Lu
d)
Nb
Y
WPG
VAG+synCOLG
ORG
e)
Rb
Y+Nb
Syn-COLG
WPG
VAG
ORG
This study
16VN08-08
16VN08-09
Troodos intra-oceanic forearc
tholeiitic plagiogranite
Talkeetna intra-oceanic mature arc
intermediate to felsic rocks
(averaged value)
f)
Zr/117
A = N-MORB
B = E-MORB
C = OIB (Rift)
D = Arc-basalts
A
B
C
D
Th
Nb/16
g)
Th/Yb
Nb/Yb
Continental
Arc
Ocenic
Arc
OIB
E-MORB
N-MORB
MORB-OIB Array

2008), which commonly produce migmatites; (2) the U–Pb zircon ages of the tonalite (16VN08–08–06) and trondhjemite (16VN08–09–06) samples are identical within analytical errors, and display similarly high, positive zircon εHf(t) values (average of +14 and +15, respectively, which are slightly lower than those of the depleted mantle) (Fig. 5g). These indicate that they might be products of fractional crystallization of mafic magma derived from slab-modified mantle wedge, and were crystallized roughly simultaneously. A fractionation origin of the studied rocks seems to be also supported by the overlap of their zircon $(^{176}Hf/^{177}Hf)_i$ values (0.282773–0.282909 and 0.282822–0.282897, Table 3) with remarkably different whole–rock SiO_2 (63.68 and 74.38 wt%, respectively, Table 5) contents; (3) On the SiO_2 versus selected major elements diagrams (Figs. 6g, h, 7a, b, c, d), the studied samples display negative correlations of Al_2O_3, MgO, FeO, TiO_2, CaO and slightly positive correlation of K_2O with SiO_2 values. It is likely that these features have been resulted from fractionated crystallization of plagioclase, amphibole, biotite and Fe–Ti oxides minerals. Moreover, the studied plagiogranites show evolutionary trends overlapping with those of the Troodos intra–oceanic forearc tholeiitic plagiogranites. A fractional crystallization origin has been well established for rocks from the latter locality (Freund et al., 2014). Otherwise, the experimentally discriminating line in the TiO_2 vs. SiO_2 diagram to distinguish the petrogenesis of oceanic plagiogranites of Koepke et al. (2007) was also added into Fig. 7c for discussion. Koepke et al. (2007) suggested that the TiO_2 values of plagiogranitic veins or small stocks generated by hydrous partial melting of oceanic cumulate gabbros are low, and distribute below this line, while those plagiogranites generated by MORB differentiation (and liquid immiscibility that is very rare in nature) are relatively high, and fall above this line. Fig. 7c shows that the TiO_2 values and evolutionary trend of the Dieng Bong oceanic plagiogranites totally overlap with those of the fractional crystallization–derived, SiO_2–rich, calc–alkaline rocks in the Oytag (Jiang et al., 2008) and Talkeetna (Kelemen et al., 2014) intra–oceanic arcs, but are completely different from Fournier mid–ocean ridge plagiogranites generated by hydrous partial melting (Brophy and Pu, 2012). However, the TiO_2 concentrations of calc–alkaline plagiogranites from the Tam Ky–Phuoc Son, Oytag, and Talkeetna intra–oceanic arcs are slightly lower than those of the tholeiitic plagiogranites from the Troodos intra–oceanic forearc, and are also lower than the minimum TiO_2 contents of experimental melts formed by MORB differentiation in tholeiitic systems (Koepke et al., 2007) (Fig. 7c). These slightly low TiO_2 contents are likely due to the high water content and oxidizing condition (Ni–NiO buffer) in arc settings, which results in early stabilization of Fe–Ti oxides (e.g., titanomagnetite), leading to a transition of the MORB differentiation path from tholeiitic (dry conditions) to calc–alkalic (water–saturated), and TiO_2 depletion in the residual melts (e.g., Sisson and Grove, 1993; Berndt et al., 2005); (4) the studied rocks display flat, chondrite–normalized REE patterns with slight LREE–depletion, which is typically seen in plagiogranites generated by fractional crystallization from a hydrous oceanic arc basaltic magma (e.g., Dilek and Thy, 2006; Jiang et al., 2008; Freund et al., 2014; Haase et al., 2016). By contrast, plagiogranites formed by dehydration melting are commonly characterized by enrichment of LREEs, and a concave upwards REE pattern (e.g., Pu et al., 2014) (Fig. 8b); (5) the studied rocks show a decrease in Sr with slightly increasing Rb (Fig. 7e), which is normally attributed to fractionation of plagioclase and biotite (e.g., Halliday et al., 1991; Frost et al., 2016). Petrographic observations of abundant plagioclase as well as minor biotite and positive correlation between Ba and K displayed by the studied samples seem to support this interpretation (Fig. 7f). Furthermore, the roughly parallel to the MALI boundary trending (Fig. 6c), the variably negative Eu anomalies (Fig. 8b) and high Pb/Ce and Sr/Nd ratios (Fig. 8c, Table 4) shown by the studied samples lend further support to the above interpretations; (6) from zircon chemistry, Pietranik et al. (2017) suggested that the variations of Hf concentration in zircon can be roughly related to those of Si content in the surrounding melt. Therefore, the increase of Hf values with decreasing Nb values in zircon observed in this study (Fig. 5d) is most likely related to fractionation of amphibole in the ambient melts, because of the much higher distribution coefficient of Nb in amphibole than any other major phase (e.g., Brophy, 2008). In support of this consideration, the zircon U/Yb vs. Gd/Yb diagram (Fig. 5e) also shows fractionation trends, indicating crystallization of amphibole, zircon, titanite, apatite and ilmenite (Grimes et al., 2015). This is consistent with the trends shown in the Gd/Yb vs. Ce/Yb zircon diagram (Fig. 5f), suggesting removal of ilmenite and apatite from the melts (Grimes et al., 2015).

In summary, the Dieng Bong plagiogranites were most likely to be formed by extensive fractionation of hydrous basaltic magma.

6.3. Emplacement timing

Two representative samples of the tonalite (16VN08–08–06) and trondhjemite (16VN–08–09–06) from the TPSZ yielded zircon U–Pb ages of 502.1 ± 6.0 Ma and 518.5 ± 7.1 Ma, respectively, indicating emplacement during the Cambrian. In the TPSZ and surrounding areas, records of early Paleozoic arc–related magmatism are limited, and these are the oldest magmatic zircons that have been documented so far. Gardner et al. (2017) published a zircon U–Pb age of ca.470 Ma for arc–like magmatic rocks located to the south of the TPSZ (Fig. 1). Tri and Khuc (2011) also reported some early Ordovician arc–like mafic, dioritic and granitic rocks in the northern KT, but direct age constraint is lacking. However, the most common magmatic rocks in this area range in age from ca. 450 to ca. 400 Ma, and have been interpreted as products of arc– or collision–related processes (e.g., Usuki et al., 2009; Shi et al., 2015). These rocks either cross–cut the TPSZ (e.g., Tri and Khuc, 2011; Tran et al., 2014) or intrude in the KT (e.g., Carter et al., 2001; Nagy et al., 2001) and TST (e.g., Carter et al., 2001; Vuong et al., 2004; Shi et al., 2015; Hieu et al., 2016; Nguyen and Tran, 2016; S.F. Wang et al., 2016) (Fig. 1). The available geochronological data indicate flare–ups of arc–related magmatism during early Paleozoic, suggesting a major period of tectono–magmatic activity in the central Vietnam. The geochronology data reported in the present study are likely records of this early tectonic event.

6.4. Tectonic setting

The Dieng Bong calc–alkaline plagiogranites have coherent patterns in N–MORB–normalized multi–element diagrams (Fig. 8c), and show depletion in LREE relative to HREE, and are comparable to those of MORB. However, the enrichment of LILEs (e.g. Cs, Rb, Ba, Pb, K) relative to HFSEs (e.g., Nb, Ti) (Fig. 8c) distinguish these rocks from those formed in mid–ocean ridge or intraplate, but rather similar to subduction–related volcanic rocks (e.g., Kelemen et al., 1993, 2003). Relatively high Th/Nb (0.25–0.59), La/Nb (1.03–2.46), Ba/La (15–103), Pb/Ce (0.11–0.27) and Sr/Nd (16–32) (Table 5) also suggest the involvement of subducted components into the magma generation (Kelemen et al., 2014; Chiaradia, 2015). Moreover, the arc–like features are also evident on the tectonic discrimination diagrams including Nb vs. Y, Rb vs. Y + Nb (Pearce et al., 1984), Zr/117–Th–Nb/16 (Wood et al., 1979)

Fig. 8. (a) Sr/Y vs. Y diagram, note that none of our samples lie within the high Sr/Y "adakite" field defined by Defant and Drummond (1990); (b) chondrite–normalized rare–earth element diagram (the normalization values from Sun and McDonough, 1989). Note that the patterns of our samples are very similar to those of the Troodos fractional crystallization–origin plagiogranites (Freund et al., 2014), but totally different from those of the Asogo dehydration melting–origin plagiogranites (Pu et al., 2014); (c) extended trace–element diagrams, concentrations are normalized to N–MORB (Dilek and Furnes, 2011). Note that patterns of our samples are remarkably similar to those of the Talkeetna rocks (Kelemen et al., 2014). Tectonic discrimination diagrams: (d) Nb vs. Y and (e) Rb vs. Y + Nb (after Pearce et al., 1984), VAG: volcanic arc granite, Syn–COLG: syn–collisional granite, WPG: within–plate granite, ORG: ocean ridge granite; (f) Zr/117–Th–Nb/16 (after Wood et al., 1979); (g) Th/Yb vs. Nb/Yb (after Pearce, 2014). Note the distribution of our samples is very similar to that of the Troodos and Talkeetna intra–oceanic arc rocks.

and Th/Yb vs. Nb/Yb (Pearce, 2014) (Fig. 8d, e, f, g). Generally, the subducting slab materials (i.e., sediments and altered oceanic crust) can be partial melted and dehydrated at various portions of the slab to produce the melts and aqueous fluids, respectively. These melts/fluids then migrate upward and mix with the overlying mantle wedge to form arc magmas (e.g., Ryan and Chauvel, 2014; Schmidt and Poli, 2014). Alternately, slab compositions can be physically mixed with hydrated mantle at slab–mantle interface to form high–pressure mélange that subsequently ascend as diapirs into the mantle wedge and melts to produce arc magmas (e.g., Nielsen and Marschall, 2017; Codillo et al., 2018). Our samples show highly positive zircon εHf(t) (average of +14 and + 15) values, but are scattered and slightly below the depleted mantle values (Table 3, Fig. 5g). These demonstrate that they might have crystallized within the magma generated by mixing of sediment melts with the mantle wedge (e.g., Nielsen and Marschall, 2017). In other worlds, the parental magma of our plagiogranites were most likely derived from the mantle wedge that was slightly modified by melts and aqueous fluids released from subducting slab.

We suggest an intra–oceanic setting for the studied plagiogranites on the basis of the following observations: (1) REE patterns of the studied rocks are similar (except for Eu anomalies) to those of MORB and Troodos intra–oceanic forearc tholeiitic plagiogranites (Fig. 8b); (2) no inherited zircons are found in our samples; (3) on discrimination diagrams of zircon U/Yb vs. Hf, U/Yb vs. Yb and U vs. Y (Grimes et al., 2007), the samples mostly fall in the ocean crust field, and have U/Yb (0.09–0.33, Table 2) ratios slightly higher than that of the MOR zircons (typically <0.1) but are typical for the oceanic arc zircons (Grimes et al., 2015) (Fig. 5a, b, c); (4) their highly positive zircon εHf(t). On the other hand, the spread of data across the volcanic arc–ocean ridge fields in the Nb vs. Y and Rb vs. Y + Nb plots is a feature that has been usually seen in plagiogranites formed in an intra–oceanic arc setting (e.g., Floyd et al., 1998; Jiang et al., 2008; Freund et al., 2014) (Fig. 8d, e). This is also demonstrated in the Th/Yb vs. Nb/Yb plot (Fig. 8g) in which all the analyzed samples fall in the oceanic arc field (Pearce, 2008, 2014). Collectively, these lines of evidence suggest that the studied plagiogranites were formed in an intra–oceanic arc. This is consistent with the previously reported geological setting of the Dieng Bong Complex, which belong to intra–oceanic volcanic arc crust within the TPSZ.

6.5. Tam Ky–Phuoc Son Suture Zone evolution and tectonic implications

As mentioned above, the Hiep Duc ultramafic–mafic Complex is most likely the on–land fragments of an intra–oceanic forearc crust (i.e., forearc ophiolite) within the TPSZ (Fig. 2a, d). This is supported by several lines of evidence: (1) the presence of deep–water sedimentary rocks suggests this rock mélange was probably formed in an oceanic setting; (2) the mafic–ultramafic rocks show arc–type geochemical features, i.e., depletion in Nb, Ti and enrichment in Rb, Ba, U, Th (e.g., Izokh et al., 2006); (3) Cr# values of Cr–spinel in the peridotite are >0.5 (0.5 to 0.54, Dung et al., 2006), typical of a forearc mantle (e.g., Stern, 2010); (4) the peridotites are dominated by strongly depleted harzburgites, and are mostly serpentinized, supporting their formation in a forearc setting (e.g., Dilek and Furnes, 2011, 2014; Pearce, 2014); and (5) some boninitic rocks, which are common in forearcs (e.g., Stern, 2010), have been found within the TPSZ in the Phuoc Son area (Fig. 2a) (Nguyen, 2001). Moreover, Fig. 2a shows that the Hiep Duc Complex rocks show close affinities to the intra–oceanic volcanic arc mélange (i.e., Ngoc Hoi, Dieng Bong, Nui Vu Complexes). This indicates that they might represent the forearc and volcanic arc of an intra–oceanic arc system, generated by the subduction of an oceanic crust under another oceanic crust within the Tam Ky–Phuoc Son Ocean (TPO). In this scenario, the forearc was produced during a short time interval (<10 My) at the early stage, followed by the formation of the volcanic arc during the early Paleozoic. This is consistent with observations in the modern intra–oceanic arc systems (e.g., Stern, 2010; Ishizuka et al., 2014).

The subduction polarity of the TPO has remained uncertain. Recently, Faure et al. (2018) argued that the pre–Devonian volcano–sedimentary rocks in the north of the TPSZ experienced low metamorphic faces. In contrast, the early Paleozoic migmatites and highly metamorphic rocks abundantly occur in areas to the south of the suture. In fact, highly metamorphosed and deformed rocks often form parts of the subducted plate in many orogenic belts (e.g., Dilek and Altunkaynak, 2007, for review). Therefore, Faure et al. (2018) proposed a northward subduction for the early Paleozoic TPO. Meanwhile, Shi et al. (2015) and Gardner et al. (2017) suggested bilateral subduction models for the TPO evolution during the middle Ordovician–middle Triassic and Ordo–Silurian, respectively, based on the finding of arc–related magmatic rocks in both the TST and KT. However, direct evidence from the TPSZ is lacking. Based on the spatial configuration of the TPSZ, i.e., from south to north, accretionary (Kham Duc Complex) – forearc (Hiep Duc Complex) – volcanic arc (Ngoc Hoi, Dieng Bong, Nui Vu Complexes) (Fig. 2a), we advocate the viewpoint of Faure et al. (2018). Similar configurations have been seen in the Jurassic Talkeetna (south–central Alaska) intra–oceanic arc system (e.g., Clift et al., 2005; Kelemen et al., 2014). The northward subduction scheme is also supported by the similarities, in both age and tectonic history, between the eastern part of the TPSZ and the Kuungan Suture on Hainan Island (see below). As a result, the ca. 470 Ma arc–like magmatic rocks located in the south of the TPSZ (Gardner et al., 2017) (Fig. 1) is interpreted as nappes that have been thrust southward during continental collision. Alternatively, they might be separated from the TPSZ by a detachment fault, which triggered the exhumation of the northwest–trending Ngoc Linh metamorphic core complex (Fig. 1) south of the suture during the Triassic (e.g., Faure et al., 2018). Similar displacement on a detachment fault resulting in isostatic uplift of the lower plate has been well put forward by e.g., Spencer (1984). The middle Cambrian–early Ordovician A Vuong Formation in the north of the TPSZ (Fig. 2a) was formed in a passive continental margin setting. This indicates that the oceanic crust within the TPO was not subducted directly under the TST, at least during the deposition of this formation. The tectonic model proposed for this region during the Cambrian is shown in Fig. 9b.

Detrital zircon (e.g., Usuki et al., 2013; Burrett et al., 2014; C. Wang et al., 2016) and paleontological (e.g., Fortey and Cocks, 1998; Burrett et al., 2014) studies have revealed that the TST was connected to the Indian margin of Gondwana during the early Paleozoic. However, Nd model ages and zircon inherited ages (e.g., Lan et al., 2003), together with recent provenance studies of detrital zircon from the KT (e.g., Usuki et al., 2009; Burrett et al., 2014), have demonstrated age spectra dominated by older Grenvillian–aged (ca. 1.1–1.3 Ga) sources, which is characteristic of the Australian margin of Gondwana (Zhu et al., 2011). This provides an additional evidence for the existence of the TPO between the TST and KT during the early Paleozoic (Fig. 9a). However, the presence of late Silurian China and Australia brachiopods in the TST (e.g., Tong-Dzuy et al., 2001) suggests that the TST might be proximal to Australia at that time (e.g., Metcalfe, 2011; Usuki et al., 2013). In other words, the TPO should have been closed before the late Silurian to form the Indochina Block. This is evidenced by the presence of many ca. 460–400 Ma metamorphic rocks (e.g., Maluski et al., 2005; Roger et al., 2007; Usuki et al., 2009; Tran et al., 2014) (Fig. 1) and collision–style structures (e.g., Tran et al., 2014, 2016) along the TPSZ as well as in TST and KT. The final suturing event took place at ca. 450 Ma (Usuki et al., 2009; Faure et al., 2018) or ca. 430 Ma (Tran et al., 2014).

As for the western extension of the TPSZ, Tran et al. (2014) suggested that it likely extends northwestward along the TST into Laos. This seems to be supported by the increasing recognition of Ordo–Silurian, arc–like, magmatic rocks along the TST, which might be related to the TPSZ (e.g., S.F. Wang et al., 2016; Zhao et al., 2016) (Fig. 1). Regarding the eastern continuation of the TPSZ, it is noteworthy that

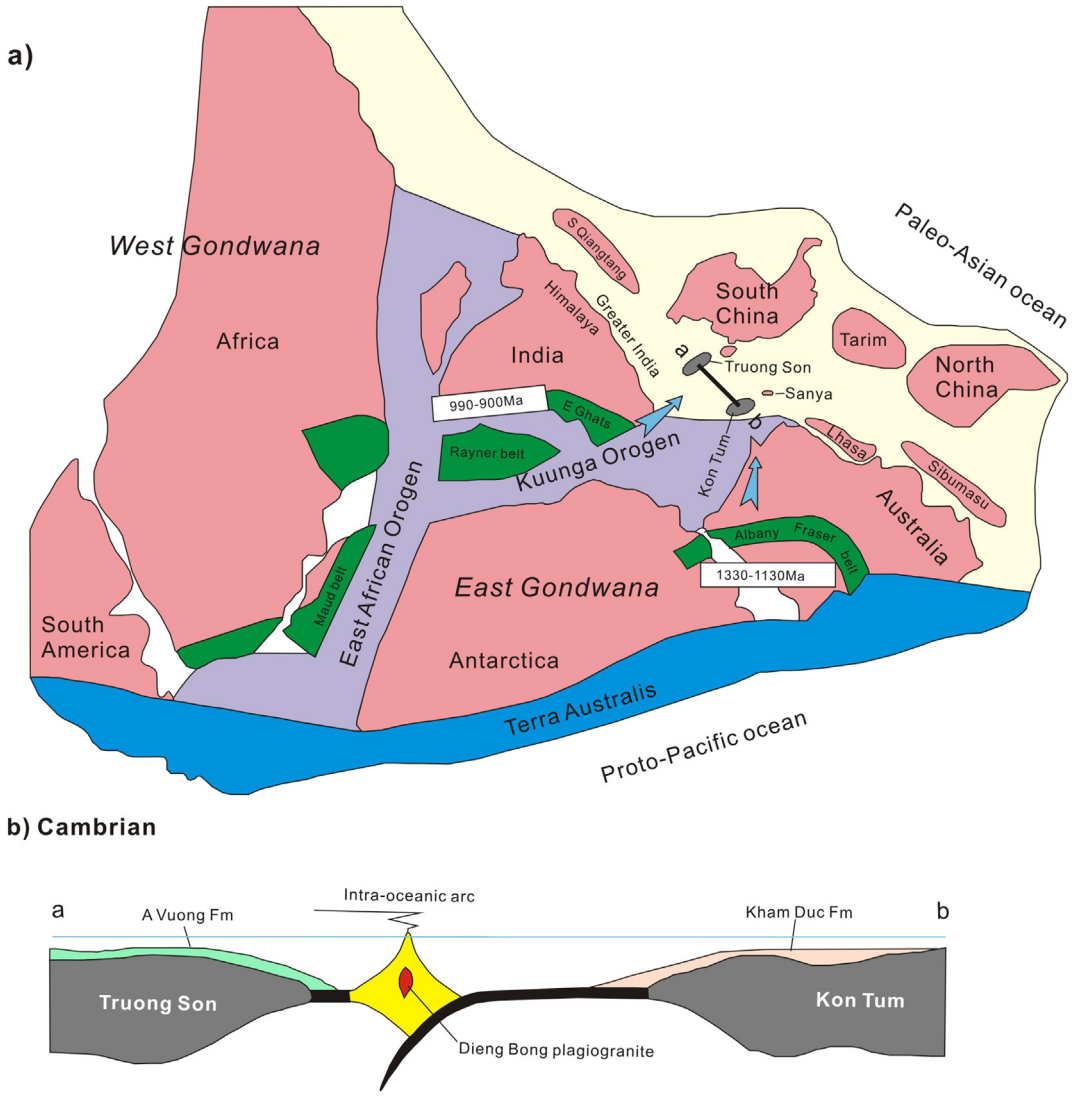

Fig. 9. (a) Schematic cartoon showing the position of Truong Son and Kon Tum Terranes at the northern margin of Indian–Australian Gondwana in the early Paleozoic (after Xu et al., 2014; Han et al., 2016; Cawood et al., 2017); (b) schematic cross–section from Truong Son to Kon Tum for the Cambrian showing the north–dipping subduction within the Tam Ky–Phuoc Son Ocean.

Indochina were separated from the South China Block by the Song Ma Ocean during late Paleozoic–early Mesozoic (e.g., Liu et al., 2012; Metcalfe, 2013; Zhang et al., 2014) (Fig. 1); the Song Ma ocean has been considered a branch or back–arc basin of the main Paleo–Tethyan Ocean (e.g., Metcalfe, 2013; Wang et al., 2017). However, irrespective of the nature of the Song Ma Ocean, the paleo–position of Indochina relative to South China before and after the opening of this ocean seems to be stable without noticeable variation (e.g., see Cocks and Torsvik, 2013; Lai et al., 2014 and references herein for discussion).

It is important to point out that, since the Tertiary, the Indochina block has been offset ca. 600 km southeastward along the Red River shear zone (e.g., Leloup et al., 1995; Wang et al., 1998; Sato et al., 1999), which has been accompanied by a maximum of 10–15 degree clockwise rotation (Yang and Besse, 1993) relative to the South China Block. Interestingly, by recovering Indochina to its pre–Tertiary position (Carter and Bristow, 2003), the TPSZ completely matches with the Kuungan Suture between the Qiongzhong and Sanya blocks on Hainan Island (Figs. 1, 9a). The Kuungan Suture also incorporates remnants of an early Paleozoic intra–oceanic arc system which is believed to have formed above a north–dipping subduction zone during the final assembly of Gondwana (e.g., Ding et al., 2002; Xu et al., 2007, 2008; Xu et al., 2014; Cawood et al., 2017).

7. Conclusions

Our new results obtained in this study, combined with previously published data from the TPSZ, allow the following conclusions to be drawn:

(1) The Dieng Bong trondhjemite and tonalite within the TPSZ are oceanic plagiogranites, and were emplaced in the Cambrian (520–500 Ma). They were derived by extensive fractionation of hydrous basaltic magma originated from an intra–oceanic arc system, which was likely triggered by a northward subduction within the Tam Ky–Phuoc Son Ocean;
(2) The Truong Son and Kon Tum Terranes were located at the Indian and Australian margins of Gondwana, respectively, and were separated one another by the Tam Ky–Phuoc Son Ocean during the early Paleozoic. This ocean might have closed before the late Silurian, resulting in suturing of the TST with the KT to form the Indochina Block;
(3) Although the TPSZ is postulated to extend northwestwards along the Truong Son Terrane, its eastern extension most likely joins the Kuungan Suture on Hainan Island, which has recorded the final assembly of Gondwana.

Acknowledgments

This study was funded by the National Natural Science Foundation of China (41672222, 41873062) and State Key Laboratory of Geological Process and Mineral Resources (MSFGPMR201702). Part of the work was also supported by the National Project No. BDKH.13/16-20 to HTT and the Ministry of Natural Resources and Environment of Viet Nam, Project BĐKH.29/16-20 to DMT. Daniel Cox, an anonymous reviewer, and Associate Editor Sanghoon Kwon are thanked for providing critical comments which helped strengthen the paper.

References

Andersen, T., 2002. Correction of common lead in U–Pb analyses that do not report ^{204}Pb. Chemical Geology 192 (1), 59–79. https://doi.org/10.1016/S0009-2541(02)00195-X.

Barker, F., 1979. Trondhjemite; definition, environment, and hypotheses of origin. In: Barker, F. (Ed.), Trondhjemites, Dacites, and Related Rocks. Elsevier, Amsterdam, pp. 1–12 https://doi.org/10.1016/B978-0-444-41765-7.50006-X.

Berndt, J., Koepke, J., Holtz, F., 2005. An experimental investigation of the influence of water and oxygen fugacity on differentiation of MORB at 200 MPa. Journal of Petrology 46 (1), 135–167. https://doi.org/10.1093/petrology/egh066.

Blichert-Toft, J., Albarede, F., 1997. The Lu–Hf geochemistry of chondrites and the evolution of the mantle–crust system. Earth and Planetary Science Letters 148 (1), 243–258. https://doi.org/10.1016/S0012-821X(97)00040-X.

Brophy, J.G., 2008. A study of rare earth element (REE)–SiO_2 variations in felsic liquids generated by basalt fractionation and amphibolite melting: a potential test for discriminating between the two different processes. Contributions to Mineralogy and Petrology 156 (3), 337–357. https://doi.org/10.1007/s00410-008-0289-x.

Brophy, J.G., 2009. La–SiO_2 and Yb–SiO_2 systematics in mid–ocean ridge magmas: implications for the origin of oceanic plagiogranite. Contributions to Mineralogy and Petrology 158 (1), 99–111. https://doi.org/10.1007/s00410-008-0372-3.

Brophy, J.G., Pu, X.F., 2012. Rare earth element–SiO_2 systematics of mid–ocean ridge plagiogranites and host gabbros from the Fournier oceanic fragment, New Brunswick, Canada: a field evaluation of some model predictions. Contributions to Mineralogy and Petrology 164 (2), 191–204. https://doi.org/10.1007/s00410-012-0732-x.

Bui, H.B., Ngo, X.T., Khuong, T.H., Golonka, J., Nguyen, T.D., Song, Y., Itaya, T., Yagi, K., 2017. Episodes of brittle deformation within the Dien Bien Phu Fault zone, Vietnam: evidence from K–Ar age dating of authigenic illite. Tectonophysics 695, 53–63. https://doi.org/10.1016/j.tecto.2016.12.006.

Burrett, C., Zaw, K., Meffre, S., Lai, C.K., Khositanont, S., Chaodumrong, P., Udchachon, M., Ekins, S., Halpin, J., 2014. The configuration of Greater Gondwana–evidence from LA ICPMS, U–Pb geochronology of detrital zircons from the Paleozoic and Mesozoic of Southeast Asia and China. Gondwana Research 26 (1), 31–51. https://doi.org/10.1016/j.gr.2013.05.020.

Carter, A., Bristow, C., 2003. Linking hinterland evolution and continental basin sedimentation by using detrital zircon thermochronology: a study of the Khorat Plateau Basin, eastern Thailand. Basin Research 15 (2), 271–285. https://doi.org/10.1046/j.1365-2117.2003.00201.x.

Carter, A., Roques, D., Bristow, C., Kinny, P., 2001. Understanding Mesozoic accretion in Southeast Asia: significance of Triassic thermotectonism (Indosinian Orogeny) in Vietnam. Geology 29 (3), 211–214. https://doi.org/10.1130/0091-7613(2001)029<0211:UMAISA>2.0.CO;2.

Cawood, P.A., Zhao, G.C., Yao, J.L., Wang, W., Xu, Y.J., Wang, Y.J., 2017. Reconstructing South China in Phanerozoic and Precambrian supercontinents. Earth-Science Reviews https://doi.org/10.1016/j.earscirev.2017.06.001.

Chiaradia, M., 2015. Crustal thickness control on Sr/Y signatures of recent arc magmas: an Earth scale perspective. Scientific Reports 5 (1), 8115–8120. https://doi.org/10.1038/srep08115.

Clift, P.D., Draut, A.E., Kelemen, P.B., Blusztajn, J., Greene, A., 2005. Stratigraphic and geochemical evolution of an oceanic arc upper crustal section: the Jurassic Talkeetna Volcanic Formation, south–central Alaska. Geological Society of America Bulletin 117 (7–8), 902–925. https://doi.org/10.1130/B25638.1.

Cocks, L.R.M., Torsvik, T.H., 2013. The dynamic evolution of the Palaeozoic geography of eastern Asia. Earth-Science Reviews 117, 40–79. https://doi.org/10.1016/j.earscirev.2012.12.001.

Codillo, E.A., Le Roux, V., Marschall, H.R., 2018. Arc–like magmas generated by mélange–peridotite interaction in the mantle wedge. Nature Communications 9 (1), 2864–2875. https://doi.org/10.1038/s41467-018-05313-2.

Coleman, R.G., Donato, M.M., 1979. Chapter 5 – oceanic plagiogranite revisited. In: Barker, F. (Ed.), Trondhjemites, Dacites, and Related Rocks. Elsevier, Amsterdam, pp. 149–168 https://doi.org/10.1016/B978-0-444-41765-7.50010-1.

Deer, W.A., Howie, R.A., Zussman, J., 1992. An Introduction to the Rock–forming Minerals. Scientific and Technical (696 pp.).

Defant, M.J., Drummond, M.S., 1990. Derivation of some modern arc magmas by melting of young subducted lithosphere. Nature 347 (6294), 662–665. https://doi.org/10.1038/347662a0.

Department of Geology and Minerals of Vietnam (DGMVN), 1989. Geology of Vietnam. Vol. 1: Stratigraphy. Science Publisher, Hanoi (378 pp., in Vietnamese).

Dilek, Y., Altunkaynak, Ş., 2007. Cenozoic Crustal Evolution and Mantle Dynamics of Post–Collisional Magmatism in Western Anatolia. International Geology Review 49 (5), 431–453. https://doi.org/10.2747/0020-6814.49.5.431.

Dilek, Y., Furnes, H., 2011. Ophiolite genesis and global tectonics: geochemical and tectonic fingerprinting of ancient oceanic lithosphere. Geological Society of America Bulletin 123 (3–4), 387–411. https://doi.org/10.1130/B30446.1.

Dilek, Y., Furnes, H., 2014. Ophiolites and their origins. Elements 10 (2), 93–100. https://doi.org/10.1130/B30446.1.

Dilek, Y., Thy, P., 2006. Age and petrogenesis of plagiogranite intrusions in the Ankara mélange, central Turkey. Island Arc 15 (1), 44–57. https://doi.org/10.1111/j.1440-1738.2006.00522.x.

Ding, S.J., Xu, C.H., Long, W.G., Zhou, Z.Y., Liao, Z.T., 2002. Tectonic attribute and geochronology of metavolcanic rocks, Tunchang, Hainan Island. Acta Petrologica Sinica 18 (1), 83–90 (in Chinese with English abstract).

Dung, P.T., Hoa, T.T., Phuong, N.T., Anh, T.T., Nien, B.A., 2006. Characteristics of mineral composition (olivine, pyroxene, chrome spinel) of ultramafic intrusions located in the margin of the Kon Tum Block. Journal of Geology 28, 47–57 (Department of Geology and Minerals of Vietnam).

Faure, M., Nguyen, V.V., Hoai, L.T.T., Lepvrier, C., 2018. Early Paleozoic or Early–Middle Triassic collision between the South China and Indochina Blocks: the controversy resolved? Structural insights from the Kon Tum massif (Central Vietnam). Journal of Asian Earth Sciences 166, 162–180. https://doi.org/10.1016/j.jseaes.2018.07.015.

Floyd, P.A., Yaliniz, M.K., Goncuoglu, M.C., 1998. Geochemistry and petrogenesis of intrusive and extrusive ophiolitic plagiogranites, Central Anatolian Crystalline Complex, Turkey. Lithos 42 (3), 225–241. https://doi.org/10.1016/S0024-4937(97)00044-3.

Fortey, R.A., Cocks, L.R.M., 1998. Biogeography and palaeogeography of the Sibumasu terrane in the Ordovician: a review. In: Hall, R., Holloway, J.D. (Eds.), Biogeography and Geological Evolution of SE Asia. Backhuys Publishers, Leiden, the Netherlands, pp. 43–56.

Freund, S., Haase, K.M., Keith, M., Beier, C., Garbe-Schönberg, D., 2014. Constraints on the formation of geochemically variable plagiogranite intrusions in the Troodos Ophiolite, Cyprus. Contributions to Mineralogy and Petrology 167 (2), 1–22. https://doi.org/10.1007/s00410-014-0978-6.

Frost, B.R., Frost, C.D., 2008. A geochemical classification for feldspathic igneous rocks. Journal of Petrology 49 (11), 1955–1969. https://doi.org/10.1093/petrology/egn054.

Frost, B.R., Arculus, R.J., Barnes, C.G., Collins, W.J., Ellis, D.J., Frost, C.D., 2001. A geochemical classification of granitic rocks. Journal of Petrology 42 (11), 2033–2048. https://doi.org/10.1093/petrology/42.11.2033.

Frost, B.R., Frost, C.D., Beard, J.S., 2016. On silica–rich granitoids and their eruptive equivalents. American Mineralogist 101 (6), 1268–1284. https://doi.org/10.2138/am-2016-5307.

Gardner, C.J., Graham, I.T., Belousova, E., Booth, G.W., Greig, A., 2017. Evidence for Ordovician subduction–related magmatism in the Truong Son terrane, SE Laos: implications for Gondwana evolution and porphyry Cu exploration potential in SE Asia. Gondwana Research 44, 139–156. https://doi.org/10.1016/j.gr.2016.11.003.

Griffin, W.L., Pearson, N.J., Belousova, E., Jackson, S.E., O'Reilly, S.Y., van Achterberg, E., Shee, S.R., 2000. The Hf isotope composition of cratonic mantle: LAM–MC–ICPMS analysis of zircon megacrysts in kimberlites. Geochimica et Cosmochimica Acta 64 (1), 133–147. https://doi.org/10.1016/S0016-7037(99)00343-9.

Grimes, C.B., John, B.E., Kelemen, P.B., Mazdab, F., Wooden, J.L., Cheadle, M.J., Hanghøj, K., Schwartz, J.J., 2007. The trace element chemistry of zircons from oceanic crust: a method for distinguishing detrital zircon provenance. Geology 35 (7), 643–646. https://doi.org/10.1130/G23603A.1.

Grimes, C.B., Wooden, J.L., Cheadle, M.J., John, B.E., 2015. "Fingerprinting" tectono–magmatic provenance using trace elements in igneous zircon. Contributions to Mineralogy and Petrology 170 (5–6), 1–26. https://doi.org/10.1007/s00410-015-1199-3.

Haase, K.M., Freund, S., Beier, C., Koepke, J., Erdmann, M., Hauff, F., 2016. Constraints on the magmatic evolution of the oceanic crust from plagiogranite intrusions in the Oman ophiolite. Contributions to Mineralogy and Petrology 171 (5), 1–16. https://doi.org/10.1007/s00410-016-1261-9.

Halliday, A.N., Davidson, J.P., Hildreth, W., Holden, P., 1991. Modelling the petrogenesis of high Rb/Sr silicic magmas. Chemical Geology 92 (1), 107–114. https://doi.org/10.1016/0009-2541(91)90051-R.

Han, Y., Zhao, G., Cawood, P.A., Sun, M., Eizenhofer, P.R., Hou, W., Zhang, X., Liu, Q., 2016. Tarim and North China cratons linked to northern Gondwana through switching accretionary tectonics and collisional orogenesis. Geology 44 (2), 95–98. https://doi.org/10.1130/G37399.1.

Hieu, P.T., Dung, N.T., Thuy, N.T.B., Minh, N.T., Minh, P., 2016. U–Pb ages and Hf isotopic composition of zircon and bulk rock geochemistry of the Dai Loc granitoid complex in Kontum massif: implications for early Paleozoic crustal evolution in Central Vietnam. Journal of Mineralogical and Petrological Sciences 111 (5), 326–336. https://doi.org/10.2465/jmps.151229.

Hoang, N., Flower, M., 1998. Petrogenesis of Cenozoic basalts from Viet–nam: implication for origin of 'Diffuse Igneous Province'. Journal of Petrology 39 (3), 369–395. https://doi.org/10.1093/petroj/39.3.369.

Hu, Z.C., Liu, Y.S., Gao, S., Liu, W.G., Zhang, W., Tong, X., Lin, L., Zong, K.Q., Li, M., Chen, H.H., Zhou, L., Yang, L., 2012. Improved in situ Hf isotope ratio analysis of zircon using newly designed X skimmer cone and jet sample cone in combination with the addition of nitrogen by laser ablation multiple collector ICP–MS. Journal of Analytical Atomic Spectrometry 27 (9), 1391–1399. https://doi.org/10.1039/c2ja30078h.

Hutchison, C.S., 1989. Geological Evolution of South–East Asia. Oxford Science Publications (368 pp.).

Huynh, T., Tran, P.H., Le, D.P., Nguyen, K.H., Tran, D.T., Tran, C.C., 2009. Geological characteristics and forming origin of ultramafic rocks (serpentinite) of Hiep Duc Complex. Journal of Science and Technology Development 12 (10), 89–102 (in Vietnamese with English abstract).

Irvine, T.N., Baragar, W.R.A., 1971. A guide to the chemical classification of the common rocks. Canadian Journal of Earth Sciences 8 (5), 523–548. https://doi.org/10.1139/e71-055.

Ishizuka, O., Tani, K., Reagan, M.K., 2014. Izu–Bonin–Mariana forearc crust as a modern ophiolite analogue. Elements 10 (2), 115–120. https://doi.org/10.2113/gselements.10.2.115.

Izokh, A.E., Tran, T.H., Ngo, T.P., Tran, Q.H., 2006. Ophiolite ultramafic–mafic associations in the northern structure of the Kon Tum block (central Vietnam). Journal of Geology 28, 20–26 (Department of Geology and Minerals of Vietnam).

Jiang, Y.H., Liao, S.Y., Yang, W.Z., Shen, W.Z., 2008. An island arc origin of plagiogranites at Oytag, western Kunlun orogen, northwest China: SHRIMP zircon U–Pb chronology, elemental and Sr–Nd–Hf isotopic geochemistry and Paleozoic tectonic implications. Lithos 106 (3), 323–335. https://doi.org/10.1016/j.lithos.2008.08.004.

Jolivet, L., Maluski, H., Beyssac, O., Goffe, B., Lepvrier, Q., Phan, T.T., Nguyen, V.V., 1999. Oligo–Miocene Bu Khang extensional gneiss dome in Vietnam: geodynamic implications. Geology 27 (1), 67–70. https://doi.org/10.1130/0091-7613(1999)027<0067:OMBKEG>2.3.CO;2.

Jolivet, L., Beyssac, O., Goffe, B., Avigad, D., Lepvrier, Q., Maluski, H., Ta, T.T., 2001. Oligo–Miocene midcrustal subhorizontal shear zone in Indochina. Tectonics 20 (1), 46–57. https://doi.org/10.1029/2000TC900021.

Katz, M.B., 1993. The Kannack complex of the Vietnam Kontum Massif of the Indochina Block: an exotic fragment of Precambrian Gondwanaland? In: Findlay, R.H., Unrug, R., Banks, M.R., Veevers, J.J. (Eds.), Gondwana 8 – Assembly, Evolution and Dispersal. A. A. Balkema, Rotterdam, pp. 161–164

Kelemen, P.B., Shimizu, N., Dunn, D., 1993. Relative depletion of niobium in some arc magmas and the continental crust: partitioning of K, Nb, La and Ce during melt/rock reaction in the upper mantle. Earth and Planetary Science Letters 120 (3), 111–134. https://doi.org/10.1016/0012-821X(93)90234-Z.

Kelemen, P.B., Yogodzinski, G.M., Scholl, D.W., 2003. Along–strike variation in the Aleutian Island Arc: genesis of high Mg# andesite and implications for continental crust. Washington DC American Geophysical Union Geophysical Monograph vol. 138(1), pp. 223–276. https://doi.org/10.1029/138GM11.

Kelemen, P.B., Hanghøj, K., Greene, A.R., 2014. 4.21–one view of the geochemistry of subduction–related magmatic arcs, with an emphasis on primitive andesite and lower crust. Treatise on Geochemistry, second edition, pp. 749–806 https://doi.org/10.1016/B978-0-08-095975-7.00323-5.

Koepke, J., Berndt, J., Feig, S.T., Holtz, F., 2007. The formation of SiO_2–rich melts within the deep oceanic crust by hydrous partial melting of gabbros. Contributions to Mineralogy and Petrology 153 (1), 67–84. https://doi.org/10.1007/s00410-006-0135-y.

Lai, C.K., Meffre, S., Crawford, A.J., Halpin, J., Zaw, Khin, Xue, C.D., Halpin, J.A., 2014. The Western Ailaoshan Volcanic Belts and their SE Asia connection: a new tectonic model for the Eastern Indochina Terrane. Gondwana Research 26 (1), 52–74. https://doi.org/10.1016/j.gr.2013.03.003.

Lan, C.Y., Chung, S.L., Van Long, T., Lo, C.H., Lee, T.Y., Mertzman, S.A., Shen, J.J.S., 2003. Geochemical and Sr–Nd isotopic constraints from the Kontum massif, central Vietnam on the crustal evolution of the Indochina block. Precambrian Research 122 (1), 7–27. https://doi.org/10.1016/S0301-9268(02)00205-X.

Le Maitre, R.W., 1989. A Classification of the Igneous Rocks and Glossary of Terms. Blackwell, Oxford (193 pp.).

Lebas, M.J., Lemaitre, R.W., Streckeisen, A., Zanettin, B., 1986. A chemical classification of volcanic–rocks based on the total alkali silica diagram. Journal of Petrology 27 (3), 745–750. https://doi.org/10.1093/petrology/27.3.745.

Leloup, P.H., Lacassin, R., Tapponnier, P., Schärer, U., Zhong, D.L., Liu, X.H., Zhang, L.S., Ji, S.C., Phan, T.T., 1995. The Ailao Shan–Red River shear zone (Yunnan, China), Tertiary transform boundary of Indochina. Tectonophysics 251 (1-4), 3–84. https://doi.org/10.1016/0040-1951(95)00070-4.

Lepvrier, C., Maluski, H., Vuong, N.V., Roques, D., Axente, V., Rangin, C., 1997. Indosinian NW–trending shear zones within the Truong Son belt (Vietnam) Ar40–Ar39 Triassic ages and Cretaceous to Cenozoic overprints. Tectonophysics 283 (1–4), 105–127. https://doi.org/10.1016/S0040-1951(97)00151-0.

Lepvrier, C., Maluski, H., Vu, V.T., Leyreloup, A., Phan, T.T., Nguyen, V.V., 2004. The Early Triassic Indochinian orogeny in Vietnam (Truong Son Belt and Kontum Massif); implications for the geodynamic evolution of Indochina. Tectonophysics 393 (1–4), 87–118. https://doi.org/10.1016/j.tecto.2004.07.030.

Liu, Y.S., Hu, Z.C., Gao, S., Günther, D., Xu, J., Gao, C.G., Chen, H.H., 2008. In situ analysis of major and trace elements of anhydrous minerals by LA–ICP–MS without applying an internal standard. Chemical Geology 257 (1–2), 34–43. https://doi.org/10.1016/j.chemgeo.2008.08.004.

Liu, Y.S., Gao, S., Hu, Z.C., Gao, C.G., Zong, K.Q., Wang, D.B., 2010. Continental and oceanic crust recycling–induced melt–peridotite interactions in the Trans–north China orogen: U–Pb dating, Hf isotopes and trace elements in zircons from mantle xenoliths. Journal of Petrology 51 (1–2), 537–571. https://doi.org/10.1093/petrology/egp082.

Liu, J.L., Tran, M.D., Tang, Y., Nguyen, Q.L., Tran, T.H., Wu, W., Chen, J., Zhang, Z., Zhao, Z., 2012. Permo–Triassic granitoids in the northern part of the Truong Son belt, NW Vietnam: geochronology, geochemistry and tectonic implications. Gondwana Research 22 (2), 628–644. https://doi.org/10.1016/j.gr.2011.10.011.

Ludwig, K.R., 2003. User's manual for Isoplot 3.00: a geochronological toolkit for Microsoft Excel. Geochronology Center Special Publication, Berkeley, pp. 41–70.

Ma, Q., Zheng, J.P., Griffin, W.L., Zhang, M., Tang, H.Y., Su, Y.P., Ping, X.Q., 2012. Triassic "adakitic" rocks in an extensional setting (North China): melts from the cratonic lower crust. Lithos 149, 159–173. https://doi.org/10.1016/j.lithos.2012.04.017.

Maluski, H., Lepvrier, C., Leyreloup, A., Van, T.V., Thi, P.T., 2005. Ar40–Ar39 geochronology of the charnockites and granulites of the Kan Nack Complex, Kon Tum Massif, Vietnam. Journal of Asian Earth Sciences 25 (4), 653–677. https://doi.org/10.1016/j.jseaes.2004.07.004.

Martin, H., Smithies, R.H., Rapp, R., Moyen, J.F., Champion, D., 2005. An overview of adakite, tonalite–trondhjemite–granodiorite (TTG), and sanukitoid: relationships and some implications for crustal evolution. Lithos 79 (1–2), 1–24. https://doi.org/10.1016/j.lithos.2004.04.048.

Metcalfe, I., 2011. Palaeozoic-Mesozoic history of SE Asia. In: Hall, R., Cottam, M.A., Wilson, M.E.J. (Eds.), The SE Asian Gateway: History and Tectonics of the Australia–Asia Collision. Geological Society of London, Special Publications vol. 355(1), pp. 7–35. https://doi.org/10.1144/SP355.2.

Metcalfe, I., 2013. Gondwana dispersion and Asian accretion: tectonic and palaeogeographic evolution of eastern Tethys. Journal of Asian Earth Sciences 66, 1–33. https://doi.org/10.1016/j.jseaes.2012.12.020.

Metcalfe, I., Henderson, C.M., Wakita, K., 2017. Lower Permian conodonts from Palaeo–Tethys ocean plate stratigraphy in the Chiang Mai–Chiang Rai suture zone, northern Thailand. Gondwana Research 44, 54–66. https://doi.org/10.1016/j.gr.2016.12.003.

Miyashiro, A., 1974. Volcanic rocks series in island arcs and active continental margins. American Journal of Science 274 (4), 321–355.

Nagy, E.A., Maluski, H., Lepvrier, C., Scharer, U., Thi, P.T., Leyreloup, A., Tich, V.V., 2001. Geodynamic significance of the Kontum massif in central Vietnam: composite Ar–40/Ar–39 and U–Pb ages from Paleozoic to Triassic. Journal of Geology 109 (6), 755–770.

Nakano, N., Osanai, Y., Owada, M., Nam, T.N., Toyoshima, T., Binh, P., Tsunogae, T., Kagami, H., 2007. Geologic and metamorphic evolutions of the basement complexes in the Kontum Massif, central Vietnam. Gondwana Research 12 (4), 438–453. https://doi.org/10.1016/j.gr.2007.01.003.

Nakano, N., Osanai, Y., Owada, M., Hayasaka, Y., Nam, T.N., 2009. Permo–Triassic Barrovian–type metamorphism in the ultrahigh–temperature Kontum Massif, central Vietnam: constraints on continental collision tectonics in Southeast Asia. Island Arc 18 (1), 126–143. https://doi.org/10.1111/j.1440-1738.2008.00646.x.

Nakano, N., Osanai, Y., Owada, M., Tran, N.N., Charusiri, P., Khamphavong, K., 2013. Tectonic evolution of high–grade metamorphic terranes in central Vietnam: constraints from large–scale monazite geochronology. Journal of Asian Earth Sciences 73 (8), 520–539. https://doi.org/10.1016/j.jseaes.2013.05.010.

Nguyen, V.T. (Ed.), 1986. Geological Map of Vietnam 1:200000 Scale, Thua Thien Hue–Quang Ngai Sheets: E–48–XXXV (Huong Hoa), E–48–XXXVI (Thua Thien Hue), D–48–XII (Dac To), E–49–XXXI (Da Nang), D–48–VI (Ba Na), D–49–I (Hoi An), D–48–VII (Quang Ngai). Geological Survey of Vietnam, Hanoi, Vietnam.

Nguyen, X.B. (Ed.), 2001. Tectonic and Metallogeny of Southern Vietnam. Geological Archive Centre, Hanoi, Vietnam (772 pp., in Vietnamese).

Nguyen, T.G., Tran, T.H., 2016. Multiple magma intrusion along the margin of Nong Son Mesozoic basin, central Viet Nam and its regional significance. Journal of Geology 356 (3–4), 37–49 (Derpartment of Geology and Minerals of Vietnam, in Vietnamese with English abstract).

Nielsen, S.G., Marschall, H.R., 2017. Geochemical evidence for mélange melting in global arcs. Science Advances 3 (4), e1602402–e1602408. https://doi.org/10.1126/sciadv.1602402.

Owada, M., Osanai, Y., Nakano, N., Matsushita, T., Tran, N.N., Tsunogae, T., Toyoshima, T., Pham, B., Kagami, H., 2007. Crustal anatexis and formation of two types of granitic magmas in the Kontum massif, central Vietnam: implications for magma processes in collision zones. Gondwana Research 12 (4), 428–437. https://doi.org/10.1016/j.gr.2006.11.001.

Owada, M., Osanai, Y., Nakano, N., Adachi, T., Kitano, I., Tran, V.T., Kagami, H., 2016. Late Permian plume–related magmatism and tectonothermal events in the Kontum Massif, central Vietnam. Journal of Mineralogical and Petrological Sciences 111 (3), 181–195. https://doi.org/10.2465/jmps.151019b.

Pearce, J.A., 2008. Geochemical fingerprinting of oceanic basalts with applications to ophiolite classification and the search for Archean oceanic crust. Lithos 100 (1), 14–48. https://doi.org/10.1016/j.lithos.2007.06.016.

Pearce, J.A., 2014. Immobile element fingerprinting of ophiolites. Elements 10 (2), 101–108. https://doi.org/10.2113/gselements.10.2.101.

Pearce, J.A., Harris, N.B.W., Tindle, A.G., 1984. Trace element discrimination diagrams for the tectonic interpretation of granitic rocks. Journal of Petrology 25 (4), 956–983. https://doi.org/10.1093/petrology/25.4.956.

Pearce, J.A., Ernewein, M., Bloomer, S.H., Parson, L.M., Murton, B.J., Johnson, L.E., 1995. Geochemistry of Lau Basin volcanic rocks: influence of ridge segmentation and arc proximity. Geological Society of London, Special Publication 81 (1), 53–75. https://doi.org/10.1144/GSL.SP.1994.081.01.04.

Perfit, M.R., Brueckner, H., Lawrence, J.R., Kay, R.W., 1980. Trace element and isotopic variations in a zoned pluton and associated volcanic rocks, Unalaska island, Alaska: a model for fractionation in the Aleutian calcalkaline suite. Contributions to Mineralogy and Petrology 73 (1), 69–87. https://doi.org/10.1007/BF00376261.

Pietranik, A., Storey, C., Koepke, J., Lasalle, S., 2017. Zircon record of fractionation, hydrous partial melting and thermal gradients at different depths in oceanic crust (ODP Site 735B, South–West Indian Ocean). Contributions to Mineralogy and Petrology 172 (2), 1–16. https://doi.org/10.1007/s00410-016-1324-y.

Pu, X.F., Brophy, J.G., Tsujimori, T., 2014. Rare earth element–SiO_2 systematics of island arc crustal amphibolite migmatites from the Asago body of the Yakuno Ophiolite, Japan: a field evaluation of some model predictions. Contributions to Mineralogy and Petrology 168 (3), 1–12. https://doi.org/10.1007/s00410-014-1060-0.

Roger, F., Maluski, H., Leyreloup, A., Lepvrier, C., Thi, P.T., 2007. U–Pb dating of high temperature metamorphic episodes in the Kon Tum Massif (Vietnam). Journal of Asian Earth Sciences 30 (3), 565–572. https://doi.org/10.1016/j.jseaes.2007.01.005.

Ryan, J.G., Chauvel, C., 2014. 3.13. The subduction–zone filter and the impact of recycled materials on the evolution of the mantle. Treatise on Geochemistry, second edition, pp. 479–508 https://doi.org/10.1016/B978-0-08-095975-7.00211-4.

Sanematsu, K., Murakami, H., Daungsurigna, S., Vilayjack, S., Duncan, R.A., Watanabe, Y., 2011. $^{40}Ar/^{39}Ar$ ages of granitoids from the Truong Son fold belt and Kontum massif in Laos. Journal of Mineralogical and Petrological Sciences 106 (1), 13–25. https://doi.org/10.2465/jmps.091216.

Sato, K., Liu, Y., Zhu, Z., Yang, Z., Otofujii, Y., 1999. Paleomagnetic study of middle Cretaceous rocks from Yunlong, western Yunnan, China: evidence of southward displacement of Indochina. Earth and Planetary Science Letters 165 (1), 1–15. https://doi.org/10.1016/S0012-821X(98)00257-X.

Sawyer, E.W., 2008. Atlas of migmatites. The Canadian Mineralogist, Special Publications vol. 9. NRC Research Press, Ottawa (371 pp.).

Scherer, E., Munker, C., Mezger, K., 2001. Calibration of the lutetium–hafnium clock. Science 293 (5530), 683–687. https://doi.org/10.1126/science.1061372.

Schmidt, M.W., Poli, S., 2014. 4.19. Devolatilization during subduction. Treatise on Geochemistry, second edition, pp. 669–701 https://doi.org/10.1016/B978-0-08-095975-7.00321-1.

Segal, I., Halicz, L., Platzner, I.T., 2003. Accurate isotope ratio measurements of ytterbium by multiple collection inductively coupled plasma mass spectrometry applying erbium and hafnium in an improved double external normalization procedure. Journal of Analytical Atomic Spectrometry 18 (10), 1217–1223. https://doi.org/10.1039/B307016F.

Shi, M.F., Lin, F.C., Fan, W.Y., Deng, Q., Cong, F., Tran, M.D., Zhu, H., Wang, H., 2015. Zircon U–Pb ages and geochemistry of granitoids in the Truong Son terrane, Vietnam: tectonic and metallogenic implications. Journal of Asian Earth Sciences 101, 101–120. https://doi.org/10.1016/j.jseaes.2015.02.001.

Sisson, T.W., Grove, T.L., 1993. Experimental investigations of the role of H2O in calc–alkaline differentiation and subduction zone magmatism. Contributions to Mineralogy and Petrology 113 (2), 143–166. https://doi.org/10.1007/BF00283225.

Spencer, J.E., 1984. Role of tectonic denudation in warping and uplift of low–angle normal faults. Geology 12 (2), 95–98. https://doi.org/10.1130/0091–7613(1984)12<95:ROTDIW>2.0.CO;2.

Stern, R.J., 2010. The anatomy and ontogeny of modern intra–oceanic arc systems. In: Kusky, T.M., Zhai, M.G., Xiao, W. (Eds.), The Evolving Continents: Understanding Processes of Continental Growth. Geological Society, London, Special Publications vol. 338(1), pp. 7–34. https://doi.org/10.1144/SP338.2.

Sun, S.S., McDonough, W.F., 1989. Chemical and isotopic systematics of oceanic basalts: implications for mantle composition and processes. In: Saunders, A.D., Norry, M.J. (Eds.), Magmatism in the Oceanic Basins. Special Publication of the Geological Society of London vol. 42(1), pp. 313–346. https://doi.org/10.1144/GSL.SP.1989.042.01.19.

Tong-Dzuy, T., Boucot, A.J., Rong, J.Y., Fang, Z.J., 2001. Late Silurian marine shelly fauna of central and northern Vietnam. Geobios 34 (3), 315–338. https://doi.org/10.1016/S0016-6995(01)80079-6.

Tran, H.T., Zaw, K., Halpin, J.A., Manaka, T., Meffre, S., Lai, C.K., Lee, Y., Le, H.V., Dinh, S., 2014. The Tam Ky–Phuoc Son shear zone in Central Vietnam: tectonic and metallogenic implications. Gondwana Research 26 (1), 144–164. https://doi.org/10.1016/j.gr.2013.04.008.

Tran, H.T., Bui, T.M., Nguyen, Q.H., Nguyen, T.G., Hoang, N.T.D., 2016. Strucutral feature of the southeastern portion of the Tam Ky–Phuoc Son suture zone and its significance for the regional tectonic framework. Journal of Geology 356 (3–4), 7–18 (Derpartment of Geology and Minerals of Vietnam, in Vietnamese with English abstract).

Tri, T.V., Khuc, V. (Eds.), 2011. Geology and Earth Resources of Vietnam. Publishing House for Science and Technology, Hanoi, Vietnam (645 pp.).

Usuki, T., Lan, C.Y., Yui, T.F., Iizuka, Y., van Vu, T., Tran, T.A., Okamoto, K., Wooden, J.L., Liou, J.G., 2009. Early Paleozoic medium–pressure metamorphism in central Vietnam: evidence from SHRIMP U–Pb zircon ages. Geosciences Journal 13 (3), 245–256. https://doi.org/10.1007/s12303-009-0024-2.

Usuki, T., Lan, C.Y., Wang, K.L., Chiu, H.Y., 2013. Linking the Indochina block and Gondwana during the Early Paleozoic: evidence from U–Pb ages and Hf isotopes of detrital zircons. Tectonophysics 586, 145–159. https://doi.org/10.1016/j.tecto.2012.11.010.

Vuong, N.V., Tich, V.V., Bent, H., 2004. The application of the U–Pb TIMS method to the analyses of the crystallization age of Dai Loc massif. Vietnam Journal of Earth Sciences 26, 202–207 (in Vietnam with English abstract).

Wang, P.L., Lo, C.H., Lee, T.Y., Chung, S.L., Lan, C.Y., Yem, N.T., 1998. Thermochronological evidence for the movement of the Ailao Shan–Red River shear zone: a perspective from Vietnam. Geology 26 (10), 887–890. https://doi.org/10.1130/0091-7613(1998)026<0887:TEFTMO>2.3.CO;2.

Wang, C., Liang, X., Foster, D.A., Fu, J., Jiang, Y., Dong, C., Zhou, Y., Wen, S., Van Quynh, P., 2016a. Detrital zircon U–Pb geochronology, Lu–Hf isotopes and REE geochemistry constrains on the provenance and tectonic setting of Indochina Block in the Paleozoic. Tectonophysics 677–678, 125–134. https://doi.org/10.1016/j.tecto.2016.04.008.

Wang, S.F., Mo, Y.S., Wang, C., Ye, P.S., 2016b. Paleotethyan evolution of the Indochina Block as deduced from granites in northern Laos. Gondwana Research 38, 183–196. https://doi.org/10.1016/j.gr.2015.11.011.

Wang, Y.J., Qian, X., Cawood, P.A., Liu, H.C., Feng, Q.L., Zhao, G.C., Zhang, Y.H., He, H.Y., Zhang, P.Z., 2017. Closure of the East Paleotethyan Ocean and amalgamation of the Eastern Cimmerian and Southeast Asia continental fragments. Earth-Science Reviews 2017. https://doi.org/10.1016/j.earscirev.2017.09.013.

Wood, D.A., Joron, J.L., Treuil, M., 1979. A re–appraisal of the use of trace elements to classify and discriminate between magma series erupted in different tectonic settings. Earth and Planetary Science Letters 45 (2), 326–336. https://doi.org/10.1016/0012-821X(79)90133-X.

Xu, D.R., Xia, B., Li, P.C., Chen, G.H., Ma, C., Zhang, Y.Q., 2007. Protolith natures and U–Pb sensitive high mass–resolution ion microprobe (SHRIMP) zircon ages of the metabasites in Hainan Island, South China: implications for geodynamic evolution since the late Precambrian. Island Arc 16 (4), 575–597. https://doi.org/10.1111/j.1440–1738.2007.00584.x.

Xu, D.R., Xia, B., Bakun-Czubarow, N., Bachlinski, R., Li, P., Chen, T., 2008. Geochemistry and Sr–Nd isotope systematics of metabasites in the Tunchang area, Hainan Island, South China: implications for petrogenesis and tectonic setting. Mineralogy and Petrology 92 (3), 361–391. https://doi.org/10.1007/s00710-007-0198-0.

Xu, Y., Cawood, P.A., Du, Y., Zhong, Z., Hughes, N.C., 2014. Terminal suturing of Gondwana along the southern margin of South China Craton: evidence from detrital zircon U–Pb ages and Hf isotopes in Cambrian and Ordovician strata, Hainan Island. Tectonics 33 (12), 2490–2504. https://doi.org/10.1002/2014TC003748.

Yang, Z., Besse, J., 1993. Palaeomagnetic study of Permian and Mesozoic sedimentary rocks from Northern Thailand supports the extrusion model for Indochina. Earth and Planetary Science Letters 117 (3–4), 525–552. https://doi.org/10.1016/0012-821X(93)90101-E.

Zhang, R.Y., Lo, C.H., Li, X.H., Chung, X.L., Anh, T.T., Tri, T.V., 2014. U–Pb dating and tectonic implication of ophiolite and metabasite from the Song Ma Suture Zone, Northern Vietnam. American Journal of Science 314 (2), 649–678. https://doi.org/10.2475/02.2014.07.

Zhao, T.Y., Qian, X., Feng, Q.L., 2016. Geochemistry, zircon U–Pb age and Hf isotopic constraints on the petrogenesis of the Silurian rhyolites in the Loei fold belt and their tectonic implications. Journal of Earth Science 27 (3), 391–402. https://doi.org/10.1007/s12583-016-0671-y.

Zhao, T.Y., Feng, Q.L., Metcalfe, I., Milan, L.A., Liu, G.C., Zhang, Z.B., 2017. Detrital zircon U–Pb–Hf isotopes and provenance of Late Neoproterozoic and Early Paleozoic sediments of the Simao and Baoshan blocks, SW China: implications for Proto–Tethys and Paleo–Tethys evolution and Gondwana reconstruction. Gondwana Research 51, 193–208. https://doi.org/10.1016/j.gr.2017.07.012.

Zhu, D.C., Zhao, Z.D., Niu, Y., Dilek, Y., Mo, X.X., 2011. Lhasa terrane in southern Tibet came from Australia. Geology 39, 727–730. https://doi.org/10.1130/G31895.1.

Zi, J.W., Cawood, P.A., Fan, W.M., Wang, Y.J., Tohver, E., 2012. Contrasting rift and subduction–related plagiogranites in the Jinshajiang ophiolitic mélange, southwest China, and implications for the Paleo–Tethys. Tectonics 31 (2), 166–182. https://doi.org/10.1029/2011TC002937.